Trailing edge noise model applied to wind turbine airfoils

Bertagnolio, Franck

Publication date:
2008

Document Version
Publisher's PDF, also known as Version of record

Risø-R-Report

Trailing Edge Noise Model Applied to Wind Turbine Airfoils

Franck Bertagnolio

Risø-R-1633(EN)

Risø National Laboratory
Technical University of Denmark
Roskilde, Denmark
January 2008

Author: Franck Bertagnolio
Title: Trailing Edge Noise Model Applied to Wind Turbine Airfoils
Department: Wind Energy Department

Risø-R-1633(EN)
January 2008

Abstract (max. 2000 char.):

The aim of this work is firstly to provide a quick introduction to the theory of noise generation that are relevant to wind turbine technology with focus on trailing edge noise. Secondly, the so-called TNO trailing edge noise model developed by Parchen [1] is described in more details. The model is tested and validated by comparing with other results from the literature. Finally, this model is used in the optimization process of two reference airfoils in order to reduce their noise signature: the RISØ-B1-18 and the S809 airfoils.

ISSN 0106-2840
ISBN 978-87-550-3656-7

Contract no.:
STVF 2058-03-0024

Group's own reg. no.:
1110044-00

Sponsorship:

Cover :

Pages: 53
Tables:
References: 36

Information Service Department
Risø National Laboratory
Technical University of Denmark
P.O.Box 49
DK-4000 Roskilde
Denmark
Telephone +45 46774004
bibl@risoe.dk
Fax +45 46774013
www.risoe.dk

Contents

1 Introduction

In order to increase public acceptance of wind energy in the coming years, there is a strong need to predict and reduce aerodynamic noise emitted by wind turbines. Small modifications of a given blade geometry can lead to significant reduction (or amplification) of the self-induced aerodynamic noise. Therefore, accurate noise prediction models are desirable for wind turbine airfoil design.

Since Lighthill [2] developed his acoustic analogy for describing the sound field generated by a turbulent flow, many subsequent theoretical and experimental works have allowed for the development of engineering codes to predict noise generation and propagation in various industrial contexts. The late 80s have seen the emergence of relatively simplistic models for airfoil noise prediction which were based on dimensional analysis and were tuned using experimental measurements [3]. However, these models do not take the accurate geometry of the airfoils into account. More recently, Direct Numerical Simulations of turbulent flows, as well as the acoustic waves, using Computational Fluid Dynamics have become affordable thanks to the ever increasing capabilities of modern computers. Nevertheless, this latter approach (often refered to as Computational Aero-Acoustics) remains concealed to relatively simple geometries and low Reynolds numbers. For practical engineering use, several intermediate approaches can be considered.

As far as wind turbines are concerned, there is a general agreement in the scientific community that the main source of noise originates from the scattering of the noise generated by the turbulent eddies passing the trailing edge of the blades. In this work, we will concentrate on a model [1] which directly relates the radiated noise in the far field to a description of the average turbulent quantities in the boundary layer in the vicinity of the trailing edge. As a starting point, the model is derived from an approximate solution of the set of equations of the acoustic analogy in idealized conditions. It is then combined with well-established results of isotropic turbulence and boundary layer theories. In this respect, such a model can be denoted as a semi-empirical model.

The text is organised as follows. The first part of this report deals with several aspects of the theories leading to the formulation of the trailing edge noise model that is considered. This model is exposed in details. The second part of the study is concerned with tests and validations of the model. In the last part, the model is implemented into an optimization procedure in an attempt to reduce the noise emitted by two given airfoils originally designed for wind turbine use.

2 Aeroacoustics and Trailing Edge Noise

This section provides a non-exhaustive review of trailing edge noise modeling. The intent is not to provide all details of the mathematical developments used to derive the different models, but rather to cover the main steps of these derivations in order to understand their theorerical background. The section starts with the pioneering work by Lighthill [2] and its classical acoustic analogy. In addition, some important related results that are used in the following are reported. The next part is dedicated to the approach by Amiet which was first intended for turbulent inflow noise [4], but was subsequently applied to trailing edge noise as well [5]. Thereafter, the solution method proposed by Ffowcs Williams and Hall [6] for solving trailing edge noise is introduced. These two latter sections might be skipped by the reader who wishes to concentrate only on the aspects of the theory directly related to the TNO model that is introduced later in this review. Then, the diffraction theory approach by Chase [7], and refined by Chandiramani [8], is described. The vortex theory for noise generation is introduced following Howe [9], and Brooks and Hodgson [10], yielding the main ingredients for the derivation of the above-mentioned TNO model. Following Blake [11], the wall surface turbulent pressure fluctuations are related both to the far field sound and turbulent boundary layer characteristics. These results are used to formulate the TNO model which is described in the last section.

As an heuristic introduction, the basic mechanism of trailing edge noise generation is the following. Inhomogeneities in the acoustic domain, such as the geometry of the domain (e.g. sharp edges), or abrupt changes in the physical properties of the medium (e.g. impedance discontinuities), provide a scattering mechanism whereby high-wavenumber pressure fluctuations, that can typically be found in a turbulent flow, can be converted and radiated as acoustic waves.

2.1 Lighthill Analogy and Related Solutions

The originial work of Lighthill consists in deriving a set of exact wave equations that characterizes the generation of sound whose source terms are related to turbulent structures. This equation of state can be relatively simply obtained by deriving the conservation of mass with respect to time, and by taking the divergence of the momentum equation. Combining these two equations yields to the well-known Lighthill's wave equation:

$$\Big(\frac{\partial^2}{\partial t^2} - c_0^2\nabla^2\Big)\rho = \frac{\partial^2 T_{ij}}{\partial x_i \partial x_j} + \frac{\partial q}{\partial t}$$

where c_0 is the sound velocity, ρ is the fluid density, and q is a rate of mass injection per unit volume (this term is discarded in the following). T_{ij} is the so-called Lighthill stress tensor which reads when no term is neglected:

$$T_{ij} = \rho u_i u_j + (p - c_0^2\rho)\delta_{ij} + \tau'_{ij}$$

where u_i $(i = 1, 3)$ are the velocity components, p is the fluid pressure, δ_{ij} is the Kronecker symbol, and τ'_{ij} is the viscous part of the Stokes stress tensor:

$$\tau'_{ij} = -\frac{3}{2}\mu\epsilon_{kk}\delta_{ij} + 2\mu\epsilon_{ij}$$

where μ is the fluid viscosity, and $\epsilon_{ij} = \frac{1}{2}(\frac{\partial u_i}{\partial x_j} + \frac{\partial u_j}{\partial x_i})$ is the fluid rates of strain tensor.

In the following the fluid is assumed to be isentropic, therefore the pressure fluctuations are related to the density fluctuations as:

$$p - p_0 = c_0^2(\rho - \rho_0) \tag{1}$$

where p_0 and ρ_0 are the pressure and density of the fluid at rest. In addition, the magnitude of the turbulent Reynolds stresses often dominates the viscous stresses for high Reynolds number flows. The Lighthill's equation finally reads:

$$\Big(\frac{\partial^2}{\partial t^2} - c_0^2\nabla^2\Big)(\rho - \rho_0) = \frac{\partial^2 T_{ij}}{\partial x_i \partial x_j} \tag{2}$$

where Lighthill's tensor now reduces to the turbulent Reynolds stress $T_{ij} = \rho u_i u_j$.

Lighthill's equation expresses the fact that the fluid mechanical problem of calculating the aerodynamic sound is formally equivalent to solving this stationary wave equation. The radiation is then produced by a distribution of quadrupole sources whose strength per unit volume is the Lighthill stress tensor. The region of the Reynolds stress fluctuations is usually limited to a small part of the fluid domain (typically near a moving object such as an airfoil immersed into the surrounding fluid). Outside this region, the velocity fluctuations are acoustic.

It is often convenient to perform harmonic analysis of the physical problem. Due to the class of the form of the wave equation, it is natural to use the Fourier transforms in time and/or space. Assuming a time dependence of the form $\mathrm{e}^{-\mathrm{i}\omega t}$, introducing the temporal Fourier transform of the pressure fluctuations $\hat{p}$, and using equation (1) yields the following Lighthill's wave equation in the Fourier space:

$$\big(k_0^2 + \nabla^2\big)\hat{p}(\boldsymbol{x}, \omega) = -\hat{\sigma}(\boldsymbol{y}, \omega) \tag{3}$$

where $k_0 = \omega/c_0$, and $\hat{\sigma}$ is the Fourier transform of the source term in Eq.(2).

2.1.a Kirchhoff's Integral Equation

In an *unbounded* fluid, Eq.(2) can be manipulated so that it can be recasted as the so-called Kirchhoff formulation of the acoustic wave equation as:

$$4\pi c_0^2(\rho(\boldsymbol{x}, t) - \rho_0) = \iiint_{V_0} \frac{1}{r}\Big[\frac{\partial^2(\rho u_i u_j)}{\partial x_i \partial x_j}\Big]\mathrm{d}V(\boldsymbol{y})$$

where the integration volume V_0 is the source region where turbulent fluctuations are concentrated, and $r = |\boldsymbol{x} - \boldsymbol{y}|$ is the distance between a source point $\boldsymbol{y}$ and the field point $\boldsymbol{x}$ where the noise is evaluated. In this equation, the brackets denote that the function is evaluated at the retarded time $t - r/c_0$, i.e. for any function f of space and time: $\big[f(\boldsymbol{y}, t)\big] = f(\boldsymbol{y}, t - r/c_0)$. The previous equation illustrates the fact that Lighthill source term can be interpreted as having a quadrupole nature with intensity equal to the Lighthill's tensor.

In order to simplify the evaluation of the integral in the previous equation (which can be difficult due to the retardation effects in addition to the spatial derivatives), the far field solution for outgoing waves can be reformulated as:

$$4\pi c_0^2(\rho(\boldsymbol{x}, t) - \rho_0) = \frac{\partial^2}{\partial x_i \partial x_j} \iiint_{V_0} \frac{[T_{ij}]}{r}\mathrm{d}V(\boldsymbol{y})$$

which is only valid *when solid surfaces are not present* in the considered domain.

Furthermore, assuming that the turbulent source region is small compared to r, and that the velocity of the source relative to the receiver is small compared to c_0, the following result can be obtained:

$$4\pi c_0^4(\rho(\boldsymbol{x}, t) - \rho_0) = \frac{x_i x_j}{r^3} \iiint_{V_0} \Big[\frac{\partial^2 T_{ij}}{\partial t^2}\Big]\mathrm{d}V(\boldsymbol{y})$$

It is important to note that from the previous integral equation, a general rule of similitude that governs the sound power radiated by a small region of subsonic turbulence can be derived. The classical eighth-power velocity dependence of radiated power from free turbulence reads:

$$I(r) \approx \frac{\rho_0}{(4\pi)^2} \frac{U_c^8}{c_0^5} \frac{V_0}{\Lambda r^2}$$

where U_c is the constant velocity at which turbulence is convected, V_0 is the volume of the turbulent region, and Λ is the turbulent eddies correlation length. This previous result applies to noise from free jets and wakes.

2.1.b Curle's Solution

Curle [12] extends this theory to include the effects of solid surfaces and showed that the noise radiated when a turbulent flow interacts with a solid surface is more important than the one produced within the turbulent flow, provided that the Mach number is low and the flow Reynolds number is high. The method of Curle consists in providing an integral solution to Lighthill's equation relating the volume and surface turbulent quantities (fluctuating stress tensor) to the far field density variations, and thereby the noise. In fact, it is proved that the presence of quadrupoles in the turbulent flow in the vicinity of wall radiates as a distribution of dipoles located on the surface. For a stationnary and rigid surface denoted S, the Curle's equation reads:

$$4\pi c_0^2(\rho(\boldsymbol{x},t)-\rho_0) = \frac{\partial^2}{\partial x_i \partial x_j} \iiint_V \frac{[T_{ij}]}{r} \mathrm{d}V(\boldsymbol{y}) - \iint_S \frac{1}{r}\Big[\frac{\partial(\rho u_i)}{\partial t}\Big]\mathrm{d}S_i(\boldsymbol{y}) + \frac{\partial}{\partial x_i}\iint_S \frac{1}{r}[\rho u_i u_j + \tau'_{ij} + p\delta_{ij}]\mathrm{d}S_j(\boldsymbol{y}) \quad (4)$$

where $\mathrm{d}S_i$ are the components of the elementary surface vector normal to the surface and pointing out of the fluid control volume. The third term in the right hand side of this equation is the contribution of a distribution of forces on the surface and acting as dipoles. The second term is a further contribution due to the acceleration of the body in a direction normal to its surface.

In a later publication, Ffowcs Williams and Hawkings [13] generalized the Lighthill acoustic analogy equation in order to account for moving and/or deforming objects. An arbitrary function of space is introduced such that applying the Heavyside step function to it gives 0 inside the body, and 1 outside in the fluid domain. However, these developments will not be presented here as they are not relevant for the subsequent trailing edge noise theory that will be exposed.

In the following of this work, p and ρ will always denote the pressure and density fluctuations as we are here only interested in the propagation of acoustic waves due to turbulent fluctuations of the fluid flow which is assumed to be otherwise in a steady state (at least compared to the acoustic and turbulent time scales).

2.2 Linearized Airfoil Theory for Turbulent Gusts

The theory that is reported in this section is in fact the base for most inflow turbulence noise prediction models. In a paper by Amiet [5], this theory was used to formulate a trailing edge noise model. The derivation of the model is reported here, even though it is not related to the TNO model that will be used in the second part of this report when performing acoustic calculations.

In a previous work, Amiet [4] relates turbulent eddies passing across the airfoil surface to the sound generated by the surface itself. The airfoil has a finite chord

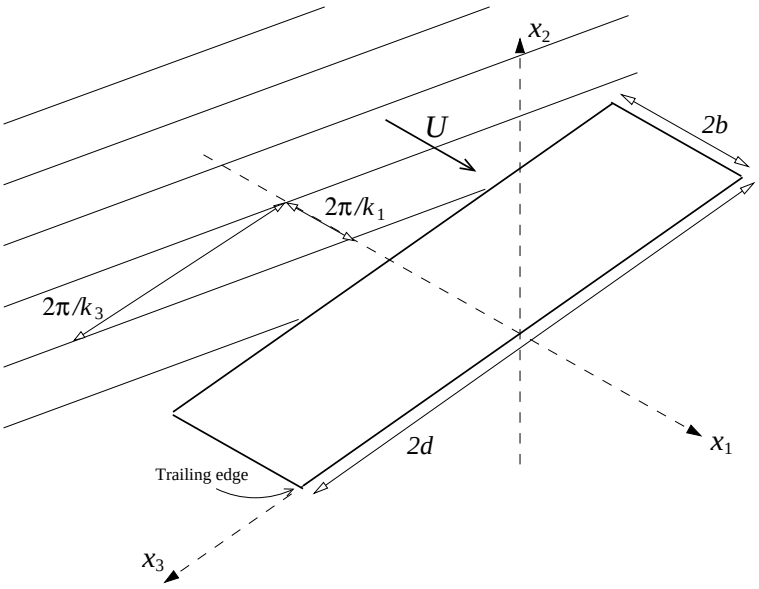

Figure 1. Skewed Gust Incident on Airfoil

$2b$ and a finite span $2d$ (see Fig.1). However, it should be noted that tip effects are neglected by assuming periodicity in the span direction. It is assumed that the turbulence is frozen and convected by the mean flow velocity U aligned with the chord direction x_1. Nevertheless, a wavefront gust can be skewed relatively to the airfoil span, i.e. it is composed of a so-called parallel component traveling in the chord direction with wavenumber k_1, and a skewed component in the span direction with wavenumber k_3. Therefore, the vertical velocity component of turbulent eddies can be described by a sum of sinusoidal gusts of the form:

$$u_{2g}(x_1, x_3, t) = v_0 \, \mathrm{e}^{\mathrm{i}(k_1(x_1 - Ut) + k_3 x_3)}$$

where v_0 is the amplitude of the gust component. The pressure jump at a given point on the airfoil encoutering the previous gust integrated over all wave number reads:

$$\Delta P(x_1, x_3, t) = 2\pi\rho_0 U b \, v_0 \iint_{-\infty}^{+\infty} \widehat{\widehat{u_2}}(k_1, k_3) \, g(x_1, k_1, k_3) \, \mathrm{e}^{\mathrm{i}(k_3 x_3 - k_1 U t)} \, \mathrm{d}k_1 \, \mathrm{d}k_3$$

where $g(x_1, k_1, k_3)$ is the transfer function between turbulent velocity and airfoil pressure jump that can be computed analytically for a flat plate of infinite span [14], and $\widehat{\widehat{u_2}}$ is the Fourier transform (in both x_1- and x_3-directions) of the turbulent vertical velocity component in the coordinate system moving with the flow, which does not depend on time because of the frozen turbulence assumption. The Fourier transform of the previous equation in time yields:

$$\Delta \hat{P}(x_1, x_3, \omega) = 2\pi\rho_0 b \int_{-\infty}^{+\infty} \widehat{\widehat{u_2}}(K_1, k_3) \, g(x_1, K_1, k_3) \, \mathrm{e}^{\mathrm{i}k_3 x_3} \, \mathrm{d}k_3 \tag{5}$$

where $K_1 = -\omega/U$ expresses the fact that a given frequency component of the pressure jump is produced by the $-\omega/U$ value of the chordwise turbulence wavenumber. Note that the integration relatively to k_1 has disappeared in the latter equation when performing the Fourier transform over time. This is due to the fact that only the complex exponential term depended on time in the former integral (thanks to the frozen turbulence assumption), leaving only the K_1 wavenumber component.

Since turbulence is a random quantity, the cross-Power Spectral Density (PSD) of the pressure jumps between two points $\boldsymbol{x}$ and $\boldsymbol{y}$ on the airfoil surface can be

written as:

$$S_{PP}(x_1, x_3, y_1, y_3, \omega) = \lim_{T\to\infty} \left\{ \frac{\pi}{T} E\big(\Delta\hat{P}^*(x_1, x_3, \omega)\, \Delta\hat{P}(y_1, y_3, \omega)\big) \right\}$$

where E denotes the expectation (or ensemble average) operator. Therefore, by using the time-Fourier transform of the pressure jumps as in Eq.(5), and evaluating the statistical expectation of the product of these spectra at two points on the surface, the cross-PSD of the pressure jumps between these two points can be related to the energy spectrum of the turbulence as:

$$S_{PP}(x_1, y_1, \Delta_3, \omega) = (2\pi\rho_0 b)^2\, U \int_{-\infty}^{\infty} g^*(x_1, K_1, k_3) g(y_1, K_1, k_3) \times \Phi_{22}(K_1, k_3)\, \mathrm{e}^{\mathrm{i}k_3\Delta_3}\, \mathrm{d}k_3 \quad (6)$$

where $\Phi_{22}(K_1, k_3)$ is the energy spectrum of the vertical velocity fluctuations integrated over all wave numbers in the direction normal to the surface. Here, $\Delta_3 = y_3 - x_3$ is the spanwise separation of the two points considered (homogeneity in spanwise direction is assumed). It should be noted that isotropic turbulence theory in combination with the Karman spectrum model yields the following expression for the previous spectrum:

$$\Phi_{22}(k_1, k_3) = \frac{4\,\overline{u^2}}{9\pi k_e^2} \frac{(k_1/k_e)^2 + (k_3/k_e)^2}{(1 + (k_1/k_e)^2 + (k_3/k_e)^2)^{7/3}}$$

where k_e is the wave number of energy-carrying eddies which can directly be related to the integral length scale of the turbulence, and $\overline{u^2}$ is the intensity of the turbulence.

The acoustic response of the airfoil to this distribution of pressure jumps across the airfoil surface is given by the theories of Kirchhoff and Curle [12, 11]. These state that the far-field noise can be modelled by a distribution of dipoles over the airfoil surface equal in strength to the force exerted on the surface. The far-field sound produced by a point force of strength $F(x_1^d, x_3^d, \omega)\mathrm{e}^{\mathrm{i}\omega t}\boldsymbol{i}_2$ ($\boldsymbol{i}_2$ is the unit vector in the vertical direction) in a stream of Mach number M reads:

$$P_F(x_1, x_2, x_3, \omega; x_1^d, x_3^d) = \frac{\mathrm{i}\omega x_2 F(x_1^d, x_3^d, \omega)}{4\pi c_0 \sigma^2} \mathrm{e}^{\mathrm{i}\omega\left(t + \frac{M(x_1 - x_1^d - \sigma)}{c_0\beta^2} + \frac{x_1 x_1^d + x_3 x_3^d \beta^2}{c_0 \beta^2 \sigma}\right)}$$

where $\sigma = \sqrt{x_1^2 + \beta^2(x_2^2 + x_3^2)}$ and $\beta = \sqrt{1 - M^2}$. In our case, the force F identifies with the pressure difference between the upper and lower surfaces of the airfoil which cross-PSD is specified by Eq.(6). Thus, integrating the previous result over the airfoil surface area, multiplying by its complex conjugate, taking the expected value, and finally substituting the cross-PSD of the pressure jumps from Eq.(6), the PSD of the far-field noise S can be related to the cross-PSD of the airfoil loading (by letting the airfoil span tends to infinity) as:

$$S_{FF}(x_1, x_2, 0, \omega) \to \left(\frac{\omega x_2 \rho_0 b}{c_0 \sigma^2}\right)^2 \pi U d\, |\mathcal{L}(x_1, K_1, 0)|^2 \Phi_{22}(K_1, 0) \quad \text{as } d \to \infty \quad (7)$$

where the observer has been assumed to be located in the plane $x_3 = 0$. The chordwise integral of the surface loading is defined here as:

$$\mathcal{L}(x_1, K_1, k_3) = \int_{-b}^{b} g(x_1^d, K_1, k_3) \mathrm{e}^{-i\omega \frac{x_1^d (M - x_1/\sigma)}{c_0 \beta^2}}\, \mathrm{d}x_1^d$$

which reduces to the sectional lift loading for small frequencies (since the complex exponent is small). Note that in Eq.(7), only the $k_3 = 0$ gusts contribute to the sound. Skewed gusts give cancelling effects and make no contribution to the sound in the plane $x_3 = 0$. A similar, though more complicated result, can be established for $x_3 \neq 0$ with additional assumptions.

By introducing the cross-correlation length $l_3(\omega)$ (which also denotes the integral length scale of turbulence) as a function of frequency, which by definition is related to the PSD of the vertical velocity fluctuations $S_{22}(\omega)$ through integration of Φ_{22} with respect to k_3, Eq.(7) can be rewritten as:

$$S_{FF}(x_1, x_2, 0, \omega) \rightarrow \left(\frac{\omega z \rho_0 b M}{\sigma^2}\right)^2 d\,|\mathcal{L}(x_1, K_1, 0)|^2 l_3(\omega) S_{22}(\omega) \quad \text{as } \Lambda \rightarrow \infty \quad (8)$$

where the parameter $\Lambda = MK_1 d$ has to be assumed large enough to allow for simplifications in the previous formula.

The previous equation is a general result for airfoil generated noise under the influence of an incoming turbulent flow. However, the same theory can be applied to trailing edge noise by considering the airfoil as a semi-infinite half-plane with a trailing edge, but no leading edge. The result of Curle (see Eq.4) for an infinite plane is considered. The solution for our problem is divided into two parts: one for the classic case of the infinite plane containing both the quadrupole and the dipole distributions, and one which will exactly cancel the dipole distribution on the fictitious airfoil extension downstream of the trailing edge, satisfying at the same time the Kutta condition at the trailing edge and the non-penetration of the wall upstream the trailing edge. The sum of the two conditions then solves the problem of a stationary turbulence field convected past the trailing edge.

The skewed gust contribution is discarded, and assuming that each far field noise frequency ω is related to a single convective velocity U, and thus the single wavenumber $K_1 = \omega/U$, an expression for the surface integral loading $\mathcal{L}$, and thereby the far field noise can be deduced. Details of the solution can be found in Amiet [5].

More recently, Casper and Farassat [15] use their so-called "Formulation 1B" of the Ffowcs Williams-Hawkings equation for acoustic problems in domains containing moving objects, and combine it with Amiet approach to formulate a model for trailing edge noise that match very well the experimental results by Brooks and Hodgson [10].

2.3 Lighthill Acoustic Analogy Applied to Trailing Edge Noise

2.3.a Ffowcs Williams and Hall Approximate Solution

One of the first theoretical works related to trailing edge noise dates back to the paper by Ffwocs Williams and Hall [6]. Here, the solution of the Lighthill's equation expressed in the Fourier space (Eq.(3)) is searched in an unbounded domain within which a rigid thin half-plane is immersed. Using the corresponding Green's function $G(\boldsymbol{x}, \boldsymbol{x'})$ with vanishing normal derivative on the half-plane, and assuming that the turbulent Reynold stress is non-zero only within a region V_0 close to the half-plane (to ensure the convergence of the volume integral over the all space), the solution for the acoustic pressure variation reads:

$$4\pi\hat{p}(\boldsymbol{x}, \omega) = \iiint_{-\infty}^{\infty} \widehat{(\rho v_i v_j)} \frac{\partial^2 G(\boldsymbol{x}, \boldsymbol{y})}{\partial y_i \partial y_j} dV(\boldsymbol{y})$$

The function G solution of the singular Green's equation with homogeneous Neumann boundary conditions, when expressed in a cylindrical coordinates system which axis coincides with the end of the half-plane (trailing edge), can be equated with the original solution for an infinite plane, but now weighted by Fresnel integrals which derivatives (since the far field noise is related to the derivatives of the Green functions as seen in the previous equation) will turn out to magnify the noise generation.

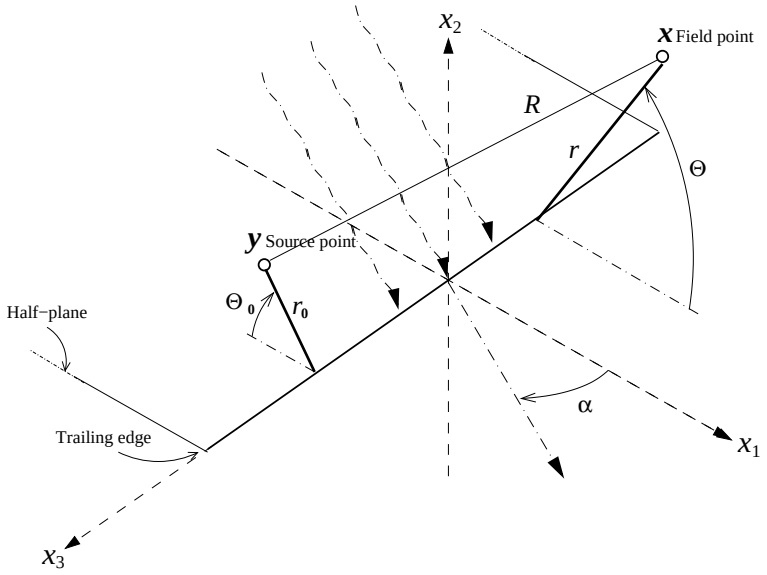

Figure 2. Coordinate System for Scattering Half-Plane

In order to be able to obtain a relative simple expression for the acoustic pressure fluctuations, some assumptions (mainly based on the relative geometric, acoustic and turbulent length scales) have to be made. In particular, attention is restricted to field points located many wavelengths both from the turbulent region and from the half-plane, that is:

$$kr >> 1 \qquad \text{and} \qquad r >> r_0$$

where k is the wavelentgth of the acoustic wave, $r = \|\boldsymbol{x}\|$ is the distance from the trailing edge to the field point where the radiated noise is evaluated, and r_0 to the turbulent noise sources (see Fig.2 for details). Mathematical manipulations yield to the following two main results:

- For eddies located very near the edge, i.e. if any point encompassed by a given eddy satisfies $2kr_0 << 1$, the acoustic pressure solution reads:

$$-4\pi\hat{p}(r,\Theta,x_3;\omega) = k^2\frac{2\mathrm{e}^{\mathrm{i}\pi/4}}{\sqrt{\pi}}(\sin\Phi)^{1/2}\cos\frac{\Theta}{2}$$
$$\times\iiint_{-\infty}^{\infty}\left(\rho\,\widehat{v_r^2}\cos\frac{\Theta_0}{2}-\rho\,\widehat{v_\Theta^2}\cos\frac{\Theta_0}{2}-2\rho\,\widehat{v_r v_\Theta}\sin\frac{\Theta_0}{2}\right)(2kr_0)^{-\frac{3}{2}}\frac{\mathrm{e}^{-\mathrm{i}kR}}{R}\,\mathrm{d}V_0$$

  where negligeable terms of series expansions of the Fresnel integrals have been eliminated thanks to the above-mentioned assumptions. R is the distance from the source point to the field point. The angle Φ is defined as $\Phi = r/\sqrt{r^2+(x_3-y_3)^2}$. Other angles are pictured in Fig.2. This results is somehow similar to the one obtained for a domain without edge. The first important difference is the presence of the factor $(2kr_0)^{-3/2}$ which produces far greater farfield acoustic pressure levels. The additional Reynolds stresses $\rho v_r v_z$ and $\rho v_\Theta v_z$ (not shown in the above equation because negligeable compared to other terms) are increased by a smaller factor $(2kr_0)^{-1/2}$, while the stress ρv_z^2 is identical to the one generated by a infinite plane (i.e. without edge).
  Additional approximations must be assumed to further simplify this integral. As pointed out by Lighthill, the turbulence can be divided into regions where the turbulent stresses are all perfectly correlated (the size of these regions

being much less than an acoustic wave length). The velocity components are divided into constant average steady component and their fluctuations which are assumed to be smaller so that second order terms can be neglected. Setting directivity factors to 1 (corresponding to the maximum scattering effect), the farfield acoustic intensity (square of the acoustic pressure spectrum) reduces to:

$$I = \frac{\rho_0 k^4 U^4 \alpha_T^2 {V_0}^2 \cos^2\alpha}{\pi^3 c_0 R^2 (k\bar{r_0})^3} \sim \rho_0 U^3 \left(\frac{U}{c_0}\right)^2 \frac{\delta^2}{R^2}$$

where α_T is the normalized turbulence intensity, V_0 is the volume of the eddy, $\bar{r_0}$ is the center of the noise generating eddy, and α is the angle of the mean flow with the x_1-direction. The well-known results that the noise intensity generated by a trailing edge increases with the fifth order of the fluid velocity is recovered. Finally, assuming that the center $\bar{r_0}$ of the noise generating eddy is equal to the correlation radius δ (defining the extent of this eddy), the farfield acoustic intensity can be recasted as:

$$I \approx \frac{\rho_0 k\, U^4 \alpha_T^2 {V_0}^2}{\pi^3 c_0 R^2 \delta^3}$$

The typical frequency of the turbulent source is of order $U/2\delta$, so that k is of order $\pi U/(c_0\delta)$, yielding again the above-mentioned fifth order law.

- For eddies remote from the edge, i.e. $kr_0 >> 1$, the development of the series expansion mainly shows that these eddies should radiate with the same intensity as those in free turbulence:

$$I \approx \frac{\rho_0 k^4 U^4 \alpha_T^2 {V_0}^2}{32\pi^2 c_0 R^2} \sim \rho_0 U^3 \left(\frac{U}{c_0}\right)^5 \frac{\delta^2}{R^2}$$

except if they are located in a specific narrow region of space. This particular case is basically ignored in the accepted theory.

Despite the numerous assumptions made to obtain these results, it seems that the fifth order scale law characteristic of trailing edge noise is well verified by experimental results.

2.4 Diffraction Theory for Trailing Edge Noise

2.4.a Chase's Pseudo-Sound Pressure

Chase [7] proposes a different approach by considering the same half-plane with a turbulent flow located only on the upper side of the plane ($x_2 > 0$). By symmetry considerations, the Green's function used to solve this problem is chosen to vanish on the downstream extension of the half-plane ($x_2 = 0,\ x_1 > 0$). It is further assumed that the turbulent quadrupoles are not present in the half-domain under the half-plane. A development somehow similar to the one proposed by Ffowcs Williams and Hall [6] is conducted. However, a particular surface wave vector of the driving turbulent surface pressure is considered:

$$p(\boldsymbol{x}^0) = p_0\, \mathrm{e}^{\mathrm{i}(k_1 x_1^0 + k_3 x_3^0)}$$

where p_0 is an arbitrary pressure amplitude, $\boldsymbol{x}^0$ denotes a (source) point on the half-plane, and $k_{1,3}$ are components of the wave vector. This pressure field is denoted in the litterature as pseudo-sound, in the sense that it represents the pressure generated by the convected turbulence in the absence of the plate. The solution of the problem now reads:

$$2\pi p(\boldsymbol{x}) = -\int_S \frac{1}{2} p(\boldsymbol{x}^0) \frac{\partial G(\boldsymbol{x^0}, \boldsymbol{x})}{\partial x_2} \mathrm{d}S$$

where S denotes the rigid half-plane. The Green's function is here chosen to satisfy the specific conditions implied by this choice for the pseudo-pressure. The factor $1/2$ in front of the pseudo-pressure has been introduced due to the presence of the wall (remind that the pseudo-pressure assumes no wall).

Introducing the known Green's function, neglecting terms due to geometrical considerations, and using known characteristics of turbulent boundary layer flow over an extended flat plate yields the following expression for the radiated sound power:

$$\Pi(\omega, \Theta, \Phi) = \frac{2kL^2}{(4\pi)^2 \rho_0 c_0} \frac{\sin \Phi}{\cos \alpha} \cos^2 \frac{\Theta}{2} S(\omega)$$

where k is the acoustic wave number, L is the spanwise extent of the turbulent flow, and Φ is the polar angle of the source projected on the edge to the field point relative to the edge axis. $S(\omega)$ is a geometric integral involving the surface pressure spectra of the pseudo-sound pressure (which reduce to the hydrodynamic pressure modelled without regard for diffraction by the adjoining rigid half-plane). This result reproduces the above one by Ffowcs Williams and Hall to within a constant factor.

Then, if the turbulent wall pressure spectrum associated to the corresponding turbulent boundary layer are given (by using for example classical turbulent boundary layer theoretical results), an approximation for the far field noise can be evaluated.

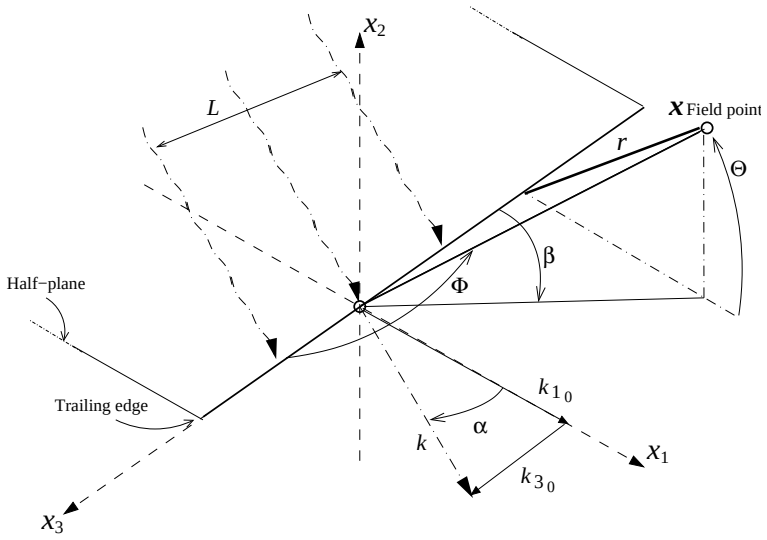

Figure 3. Geometry of Diffraction Problem

2.4.b Chandiramani's Evanescent Waves

The idea proposed by Chase (see above) is refined by Chandiramani [8]. However, instead of using the known Green's function of the problem, the introduction of pseudo-sound pressure fluctuations (i.e. the pressure that would be experienced in the domain regardless of the diffraction phenomenon) as a distribution of harmonic evanescent waves produced by convecting turbulent elements located above the plate and that have past the half-plane allows to formulate the solution as a diffraction problem. By *evanescent*, it is meant that the incident pressure waves decays exponentially as getting closer to the half-plane. The divergence of this formulation away from the wall is circumvented by the fact that the scattered

field eventually is only generated by the finite amplitude of the incident wave on the surface.

In the following, it is assumed that the incident wave has a radian frequency ω and associated time dependence $\mathrm{e}^{-\mathrm{i}\omega t}$, which is suppressed from now on. The incident evanescent wave is then expressed as:

$$p^i(\boldsymbol{x}) = \frac{P_b}{2}\mathrm{e}^{\mathrm{i}(k_{1_0}x_1+k_{3_0}x_3-k_{2_0}x_2)}$$

where k_{2_0} is positive imaginary, k_{1_0} and k_{3_0} being real. They are related as follows:

$$|k_{1_0}| > k = |\omega|/c_0\,, \quad |k_{3_0}| < k$$

$$k_{2_0} = \mathrm{i}(k_0^2 - k^2)^{1/2}\,, \quad k_0 = (k_{1_0}^2 + k_{2_0}^2)^{1/2}$$

where k is the magnitude of the acoustic wavenumber. P_b stands for the blocked pressure of the incident wave that would have been measured in the presence of a rigid half-plane (with reflection conditions) on an infinitely extended rigid surface at $x_2 = 0$. The acoustic velocity in the vertical direction x_2 associated with the incident pressure wave is given by:

$$\rho_0 \frac{\partial u_2^i(\boldsymbol{x})}{\partial t} = -\frac{\partial p^i(\boldsymbol{x},t)}{\partial x_2}$$

Combining the two previous equations yields on the rigid surface:

$$u_2^i(x_1,0,x_3) = -\frac{P_b}{2Z_a}\mathrm{e}^{\mathrm{i}(k_{1_0}x_1+k_{3_0}x_3)}$$

where $Z_a = \rho_0\omega/k_{2_0}$ is the acoustic impedance of the wall in the x_2-direction.

A similar formulation is assumed for the scattered pressure wave p^s and the x_2-component of the corresponding acoustic velocity u_2^s. Rigidity of the wall, symmetry considerations, and taking Fourier transforms of the fields yield to the following scattering problem:

- The scattering acoustic velocity as considered above can be written as:

$$u_2^s(x_1,0,x_3) = +\frac{P_b}{2Z_a}\mathrm{e}^{\mathrm{i}(k_{1_0}x_1+k_{3_0}x_3)} \qquad \text{for} \quad x_1 < 0$$

Let $\widehat{u_2^s}(k_1,0,x_3)$ being the Fourier transform of $u_2^s(x_1,0,x_3)$ with respect to the x_1-component:

$$u_2^s(x_1,0,x_3) = \int_{-\infty}^{\infty} \widehat{u_2^s}(k_1,0,x_3)\mathrm{e}^{\mathrm{i}k_1x_1}\mathrm{d}k_1$$

and $\widehat{p^s}(k_1,x_2,x_3)$ the Fourier transform of $p^s(x_1,x_2,x_3)$ in the x_1-direction:

$$p^s(x_1,x_2,x_3) = \int_{-\infty}^{\infty} \widehat{p^s}(k_1,x_2,x_3)\mathrm{e}^{\mathrm{i}k_1x_1}\mathrm{d}k_1$$

These are related as:

$$\widehat{p^s}(k1,x_2,x_3) = \pm\widehat{u_2^s}(k_1,0,x_3)\frac{\rho\omega}{k_2}\mathrm{e}^{\pm\mathrm{i}k_2x_2}$$

where the sign of the right-hand side is positive for $x_2 > 0$, and negative for $x_2 < 0$. In addition, symmetry over the plane $x_2 = 0$ yields:

$$p^s(x_1,0,x_3) = 0 \qquad \text{for} \quad x_1 > 0$$

The problem defined by the set of previous equations consists in determining $\widehat{u_2^s}(k_1,0,x_3)$ which specifies the acoustic velocity in the half domain $x_1 > 0$ and thereby the scattered pressure field∘

The previous problem can be recasted as a classical scattering problem of evanescent waves in atomic physics which solution can be derived by Wiener-Hopf theory,

which is beyond the scope of this review. The final result for the scattered pressure wave in the farfield ($k_d r >> 1$) reads:

$$p^s(x_1,x_2,x_3) = \frac{\mathrm{i}\rho_0\omega P_b}{2Z_a}\frac{\sin(\Theta/2)}{(k_d-k_{1_0})^{1/2}(k_d\cos\Theta-k_{1_0})}\frac{\mathrm{e}^{\mathrm{i}(k_d r+k_{3_0}x_3-r/4)}}{(\pi r)^{1/2}} \quad \text{for } x_2>0$$

where $x_1 = r\cos\Theta$, $x_2 = r\sin\Theta$, and $k_d = (k^2 - k_{3_0}^2)^{1/2}$. With further assumptions on the wavelengths values ($k_{1_0} >> |k| > 0$), it reduces to:

$$|p^s(x_1,x_2,x_3,t)| = \frac{P_b}{2(\pi k_{1_0} r)^{1/2}}\sin\frac{\Theta}{2}$$

By integrating over the angle Θ for both sides $x_2 > 0$ and $x_2 < 0$, the total acoustic radiated power is given by:

$$P_{\mathrm{rad}} = \frac{P_b^2}{4}\frac{1}{2\rho_0 c_0 k_{1_0}}\frac{k_d}{k}$$

It is now possible to estimate the sound diffracted by a turbulent boundary layer flow. Indeed, the previous result applies to an incident wave that would project the wavenumber vector (k_{1_0}, k_{2_0}) on an infinitely extended rigid wall at $x_2 = 0$, and yields a mean squared pressure value P_b^2 at the wall. Then, this blocked pressure is simply replaced by the wavenumber-frequency spectral density $\Phi_{P_b}(k_{1_0}, k_{3_0}, \omega)$ of a spatially homogeneous and stationary turbulent boundary layer wall pressure as it would be measured on a large rigid boundary. This result is integrated over the whole wavenumber space. Thus, we get the spectral density of the radiated acoustic power:

$$\Phi_{P_{\mathrm{rad}}}(\omega) = \iint_\Omega P_{\mathrm{rad}}(P_b/2)^{-1}\Phi_{P_b}(k_{1_0},k_{3_0},\omega)\,\mathrm{d}k_{1_0}\,\mathrm{d}k_{3_0} \tag{9}$$

where Ω denotes the portion of the wavenumber plane (k_{1_0}, k_{3_0}) for which $|k_{2_0}| < k$. From this point, the problem can be closed by determining the wall pressure spectrum Φ_{P_b}.

According to the experimental data and similarity hypothesis of Corcos [16], the wall spectral density function is assumed to be separable and take the following form:

$$\Phi_{P_b}(k_{1_0},k_{3_0},\omega) = \Phi_f(\omega)\,\Phi_1(k_{1_0})\,\Phi_3(k_{3_0})$$

where the first term in the right hand side is the frequency spectrum of the wall pressure as measured by a transducer. The two following wave number spectra express the eddy decay and convection in each direction. They are simply the Fourier transforms of the corresponding normalized cross-spectral densities in terms of spatial separation and frequency:

$$\Phi_f(\omega) \approx 9.10^{-6}\frac{q^2}{\omega}$$

$$\Phi_1(k_{1_0}) \approx \frac{L_1}{\pi}\big(1+(k_{1_0}-k_h)^2L_1^2\big)^{-1} \qquad \Phi_2(k_{2_0}) \approx \frac{L_2}{\pi}\big(1+k_{2_0}^2L_2^2\big)^{-1}$$

where $q = \rho_0 U_\infty^2/2$ is the free stream dynamic pressure, U_∞ the fress stream velocity in the x_1-direction, $L_1 \approx 9U_c/|\omega|$ and $L_2 \approx 1.4U_c/|\omega|$ are eddy-decay length scales, and $k_h = \omega/U_c$ is the hydrodynamic wave number at which $\Phi_1(k_{1_0})$ peaks. U_c is the effective convection velocity for the wall pressure. The ratio U_c/U_∞ depends somehow on the Strouhal number $\omega\delta^*/U_\infty$, where δ^* is the boundary layer displacement thickness. The previous ratio is assumed constant and takes the following value:

$$U_c/U_\infty \approx 0.6$$

for Strouhal numbers larger than 2.

The turbulent boundary layer as specified above is assumed to exist over the whole half-plane, as well as for a short distance (at least of the order of $1/k_h$) downstream the leading edge in order for the theory to be valid. After a few manipulations, the radiated pressure spectrum reads:

$$\Phi_{P_{\text{rad}}}(\omega) = \Phi_f(\omega)\frac{L_2 k}{8\rho_0 c_0 k_h} = 1.45.10^{-7}\frac{\rho_0 U_\infty^6}{(\omega c)^2}$$

where the first equality can be used if different choices are made for estimating $\Phi_f(\omega)$, L_2, or k_h.

The final result for the far field noise spectrum is obtained by integrating Eq.(9), yielding the spectral density of the scattered pressure in the far field:

$$\Phi_P^s(\omega) = \frac{L_2 k}{2\pi^2 r\, k_h}\sin^2\frac{\Theta}{2}\Phi_f(\omega)$$

2.4.c Chase's Revised Approach

In a similar way, Chase [17] introduces evanescent waves. His mathematical development are somehow slightly different from Chandiramani's approach. In particular, emphasizing the fact that we are interested in the far field noise, he considers a flow of finite lateral extent L (rather than infinite in Chandiramani's approach) by considering a distribution of wavenumber component parallel to the edge. His final result for the far field pressure spectral density (for a lateral extent much larger than the acoustic wavelength) reads:

$$S(\omega) = \frac{2M_v L}{\pi R^2}\sin^2\frac{\Theta}{2}\sin\Phi\cos\alpha\int_{-\infty}^{\infty}\Pi_i(k_1, \frac{\omega\cos\Phi}{c}, \omega)\mathrm{d}k_1$$

where the pseudo-sound spectrum Π_i is to be specified. Chase [17] selected a functional form deduced from experimental results (see also Howe [9]).

The previous result cannot explicitly be compared with Chandiramani's one as the latter makes implicit knowledge of the pseudo-sound pressure at the wall with the factor $(P_b/2)^{-1}$ (see previous section).

2.5 Howe's Vortex Method

Powell [18] was the first to derive an alternative formulation of Lighthill's acoustic analogy emphasizing the role of vortices. His approach gives a deeper insight into the mechanism that produces sound from turbulent vortices. Concentrating on trailing edge, Howe [9] develops a theory for trailing edge noise that encompasses the previous approaches.

2.5.a Acoustic Anology in Vortex Form

Under a certain number of classical assumptions, the equivalent of Lighthill's acoustic analogy theory by distributions of vortices (instead of the turbulent stress tensor) reads:

$$\left\{\frac{1}{c^2}\Big(\frac{\partial}{\partial t} + U_0\frac{\partial}{\partial x_1}\Big)^2 - \nabla^2\right\}\mathrm{B} = \mathrm{div}(\boldsymbol{\omega}\wedge\boldsymbol{V}) + \mathrm{div}(\bar{\boldsymbol{\omega}}\wedge\boldsymbol{W})$$

where $\mathrm{B} = \int(\partial p/\rho) + \boldsymbol{v}^2/2$ is the total enthalpy velocity. Note that in regions where the flow is irrotational, Bernoulli's equation implies that B is related to the velocity potential ϕ as:

$$\frac{\partial\phi}{\partial t} = -\mathrm{B}$$

In the former equation, $\boldsymbol{\omega}$ is the curl of the flow velocity $\boldsymbol{v}$, and $\boldsymbol{V}$ is the convection velocity of the associated eddies. This convection velocity is here approximated to be the local mean velocity function of x_2 only: $\boldsymbol{V} = \boldsymbol{V}(x_2)$. $\boldsymbol{W}$ is the convection

velocity for the shed vortices, which are denoted by $\bar{\boldsymbol{\omega}}$ and are assumed to be frozen during their convection.

In short, the first term in the right hand side of the equivalent acoustic equation represents the contribution to the aeroacoustic sound of the incident vorticity, and the second term of the shed vorticity. As these two contributions are expressed as the divergence of vector products, these products can be identified as the strength of dipoles which axis are aligned with these vector products. Note that the term U_0 in the left-hand side originates from the fact that the main convection direction is x_1 and that the equation has been linearized, cancelling small terms in the other directions.

Hypotheses on the orientation of these dipoles (related to the geometry of the flow and the position of the edge) yield a simplified source term for the previous equation:

$$\left\{\frac{1}{c^2}\Big(\frac{\partial}{\partial t}+U_0\frac{\partial}{\partial x_1}\Big)^2-\nabla^2\right\}B=\operatorname{div}\big(\boldsymbol{Q}\,\delta(x_2-z)\big)+\operatorname{div}\big(\boldsymbol{q}\,\delta(x_2)\big)$$

where δ is the Dirac function. The dipole strength vectors have been defined as:

$$\boldsymbol{\omega}\wedge\boldsymbol{V}=\boldsymbol{Q}\,\delta(x_2-z)\quad\text{ and }\quad\bar{\boldsymbol{\omega}}\wedge\boldsymbol{W}=\boldsymbol{q}\,\delta(x_2)$$

where the dummy variable z has been introduce for integration along the direction normal to the plane $x_2=0$.

The equation is now rewritten in term of the variable B (instead of B) defined as $\mathrm{B}=\int_0^\infty B\mathrm{d}z$. B satisfies homogeneous Neumann boundary conditions at the wall (due to the non-penetration condition for the fluid flow), and outgoing radiation condition at large distance from the wall. This results in a classical diffraction problem that can be solved with standard techniques. Note that the linearity of the problem allows for splitting the solution into $B=B_Q+B_q$ where each term corresponds respectively to the response of the incident and wake dipole sources on the right hand side of the equation. In addition, to solve this problem, the Mach number of the flow field must be assumed small compared to unity.

The solution to this problem is quite complex, and therefore is not reported here. It explicitly defines the values of B_Q and b_q as integrals over wave numbers (in the three space directions) involving the Fourier transforms (only in x_1- and x_3-directions) of the respective dipole strengths $\hat{\boldsymbol{Q}}(k_1,k_3,z)$ and $\hat{\boldsymbol{q}}(k_1,k_3,z)$.

At this point of the analysis arises an important distinction among the possible solutions by considering the enforcement of the Kutta condition or not. From the previous result, it is indeed possible to define the wake dipole strength as a function of the incident velocity depending on the specification of the Kutta condition at the trailing edge. In the absence of vortex shedding at the edge (no Kutta condition), we then have the simple result $\boldsymbol{q}\equiv 0$. Conversely, if vortex shedding is permitted in order to remove the trailing edge potential flow singularity, the flow velocity at the edge must be tangent to the wall plane, which can be expressed as:

$$\lim_{x_1\to 0^+}\frac{\partial(B_Q+b_q)}{\partial(x_2)}\Big|_{x_2=0}=0$$

From this limit, a relationship between the Fourier transforms of the dipole strengths can be deduced. This result leads to the following important conclusion: 'no edge noise is generated in the particular case in which the incident and shed vorticity convect at the same mean velocity', i.e. if $\boldsymbol{W}=\boldsymbol{V}(\boldsymbol{z})$. Indeed, in this case the shed vorticity is exactly the one that would be produced by a mirror image of the incident dipole Q in the case of an infinite rigid plane. Thereby, the far field acoustic radiation vanishes. From now on, the case for which the Kutta condition is enforced is considered.

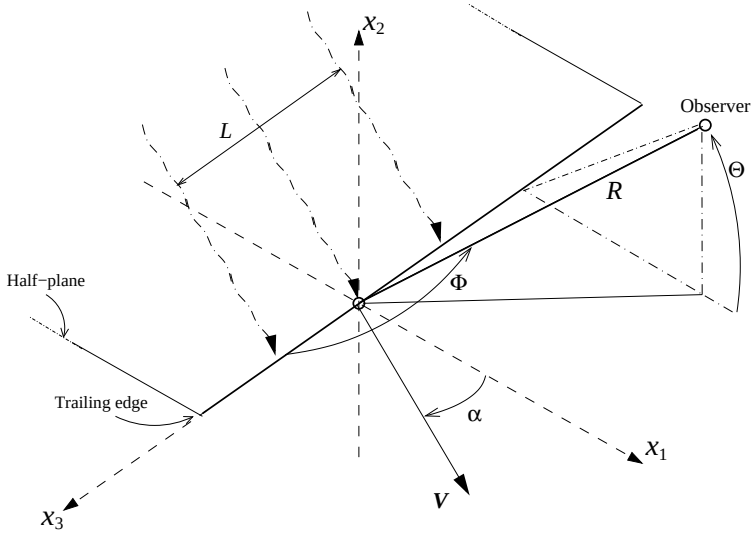

Figure 4. Half-Plane Configuration

2.5.b The Far Field Sound

A more tractable solution (than the solution of the diffraction problem mentioned above) can be obtained by relating the enthalpy to the actual acoustic perturbation. As far as the far field is considered, and at small mean flow Mach number M_0, they can be related as:

$$p_Q = \rho_0 \frac{B_Q}{1 + M_{0R}}$$

where $M_{0R} = M_0(x_1/R)$ is the component of $(M_0, 0, 0)$ in the observer direction. Then, the solution of the problem for the far field acoustic pressure p_K (where the lowerscript denotes the enforcement of the Kutta condition) reads:

$$p_K = \frac{-\mathrm{i}\rho_0 \sin(\Theta/2)\sqrt{\sin\Phi}}{R\sqrt{2}(1 + M_{0R})(1 - M_{WR})}$$
$$\times \int_{-\infty}^{\infty} \Bigg(\int_0^{\infty} \frac{\sqrt{M_{v_1}}(1 - W/V)[\boldsymbol{\mu}.\widehat{\boldsymbol{Q}}]}{(1 - M_{v_1})(1 - M_{v_1}\sin\Phi - M_{v_3}\cos\Phi)^{1/2}}$$
$$\times \exp\Big\{ -\Big(\frac{|\omega|z}{V_1}(1 - M_{v_3}\cos\Phi) + \frac{\mathrm{i}\omega}{c_0}(R - M_0 x_1 - c_0 t)\Big\}\, \mathrm{d}z \Bigg) \frac{\mathrm{d}\omega}{\omega}$$

where M_{WR} is the component of the wake convection Mach number $\boldsymbol{M}_W$ in the observer direction, M_{v_i} denotes the components of the convection Mach number $\boldsymbol{M}_v$ in the observer direction, $\widehat{\boldsymbol{Q}}$ is the Fourier transform of $\boldsymbol{Q}$ in x_1- and x_3-directions. The vector $\boldsymbol{\mu}$ is a vector involving geometric and velocity components. The fact that the acoustic pressure vanishes if incident and wake convective velocities are equal $(V = W)$ is recovered.

2.5.c Relating Wall Pressure to Far Field Sound

A similar solution for the actual fluctuating pressure field on the wall surface can be searched. At the wall surface, the enthalpy and the acoustic perturbations can be related by:

$$p_Q = \frac{\rho_0}{\omega}(\omega + \mathrm{i}\boldsymbol{W}.\nabla)B_Q$$

for each harmonic component ω. Introducing this equation into the same solution of the diffraction problem as mentioned above yields:

$$p_K = -\frac{\rho_0}{2}\iint_{-\infty}^{\infty}\left(\int_0^{\infty}\left(1+\mathrm{sgn}(x_2)\mathrm{Erf}(\sqrt{\mathrm{i}x_1[\lambda+k_1+M_0\omega_z/c]})\right)\right.$$
$$\left.\times\frac{\boldsymbol{\mu}(\boldsymbol{V}-\boldsymbol{W})(\boldsymbol{\mu}.\widehat{\boldsymbol{Q}})}{\omega_z\gamma(k_1)}\exp\left\{\mathrm{i}(k_1x_1+k_3x_3+z\gamma(k_1)-\omega_z t)\right\}\mathrm{d}z\right)\mathrm{d}k_1\,\mathrm{d}k_3$$

where the lowerscript K denotes the fact that the Kutta condition has been enforced. λ and $\gamma(k_1)$ are functions of geometric and velocity components, and $\omega_z = \boldsymbol{\mu}.\boldsymbol{V}(z)$. In the previous result, the error function[1] Erf characterizes the diffration by the trailing edge. The value $\mathrm{sgn}(x_2)=\pm 1$ depends on the side of the plane which is considered (positive for the upper side). Considering the asymptotic limit of the error function, it is easy to see that the pressure fluctuations rapidly tend to zero as $x_1 \to -\infty$ on the lower surface, and the classical pressure doubling of the pseudo-sound pressure fluctuations is recovered on the upper side. This formula gives as well the pressure fluctuations in the wake if the error function is discarded and provided that there is no mean shear in the wake. The result that have been obtained is actually a generalization of Chase's result [17].

In order to define a simple relation between surface pressure fluctuations and those in the acoustic far field, only points located in the wake or for which x_1 is small, i.e. points on the plane close to the trailing edge well within the hydrodynamic wavelength, are considered. In this case, the error function contribution can be neglected. Then, the stationarity of the pressure fluctuations as a random process can be assumed, and the spectrum $\Pi_K(k_1,k_3,\omega)$ of the previous surface pressure fluctuation defined as:

$$< p_K(x_1,x_3,t)\,p_K(x_1+X_1,x_3+X_3,t+\tau) >$$
$$= \int_{-\infty}^{\infty}\Pi_K(k_1,k_3,\omega)\mathrm{e}^{\mathrm{i}(k_1X_1+k_3X_3-\omega\tau)}\,\mathrm{d}k_1\,\mathrm{d}k_3\,\mathrm{d}\omega$$

may be introduced. This spectrum is nothing but the spectrum of the pseudo-sound pressure fluctuations considered in the evanescent wave approach by Chandiramani [8] (see section 2.4.b). It can directly be related to the spectrum of the incident dipole strength by some equation. By considering this relation in perspective of the equations defining p_K on the wall and p_K in the far field, the final relation between the far field acoustic spectrum and the pseudo-sound wave number spectrum can be obtained:

$$S_K(\omega) = \frac{2\omega L}{\pi R^2 c_0}\,\frac{\sin\Phi\,\sin^2(\Theta/2)\,\cos\alpha}{(1+M_{0R})^2(1-M_{WR})^2}$$
$$\times\int_{-\infty}^{\infty}\frac{\Pi_K(k_1,\omega\cos\Phi/c_0,\omega)}{|\boldsymbol{\mu}.\boldsymbol{n}|(1-M_{vR})^2(1-M_{v_1}\sin\Phi)}\,\mathrm{d}k_1$$

where $\boldsymbol{\mu}=(k_1,\omega\cos\Phi/c_0)$, M_{vR} is the component of the eddy convection Mach number $(\omega/c_0\boldsymbol{\mu}.\boldsymbol{n}).\boldsymbol{n}$ in the observer direction, and $M_{v_1}=(\omega/c_0\boldsymbol{\mu}.\boldsymbol{n})\cos\alpha$. Again this result is a generalization of Chase's result [17].

As showed by Brooks and Hodgson [10], if the mean flow direction is perpendicular to the trailing edge ($\alpha = 0$), the observer is located in the same plane perpendicular to the trailing edge axis as the source ($\Phi=90^o$), and the observer is located right above the trailing edge ($\Theta=90^o$), then the result of Howe becomes:

$$S_K(\omega) = \frac{\omega L}{2\pi R^2 c_0}\int_{-\infty}^{\infty}\frac{\Pi_K(k_1,0,\omega)}{|k_1|(1-k_1\omega/c_0)}\,\mathrm{d}k_1 \qquad (10)$$

[1] The error function is defined as: $\mathrm{Erf}(x) = (2/\sqrt{\pi})\int_0^{x^2}\mathrm{e}^{-t^2}\mathrm{d}t$

In this conditions (which are those of the experiment conducted by Brooks and Hodgson [10]), a very good agreement between the latter formula on one side, and measurements of both surface pressure near the trailing edge and far field noise on the other side was found.

2.5.d Relating Wall Pressure to Turbulence Structure

To complete a useful trailing edge noise model from the previous results, it is still necessary to provide an analytical or experimental description of the wall pressure fluctuations near the trailing edge. In a broader perspective, this problem has been extensively studied as part of the turbulent boundary layer theory. Indeed, turbulent boundary layer will typically induce random pressure fluctuations, which convected over a wall surface will generate noise. Note that this mechanism is not restricted to trailing edge noise, but involves as well spatially extended structures vibrations and noise generation relevant for configurations such as aircraft fuselages, sonar domes, ducts, etc...

Surface Pressure Power Spectrum The first step in determining the surface pressure fluctuation spectrum consists in deriving an expression for the Fourier transform of these fluctuations related to the characteristics of turbulence in the boundary layer. The derivation followed by Blake [11] is reported here. It is based on classical turbulent boundary layer theory results (in order to define the source term for the Reynolds averaged fluctuation for Lighthill's equation) combined with the methodology for solving Lighthill's equation as proposed by Ffwocs Williams [19].

By combining the acoustic approximation with the Lighthill's equation, an equation relating the pressure fluctuations p to the turbulent shear stress is obtained:

$$\frac{1}{c_0}\frac{\partial^2 p}{\partial t^2} - \nabla^2 p = \frac{\partial^2 \rho_0 (u_i u_j - \overline{u_i u_j})}{\partial y_i \partial y_j} \tag{11}$$

Note that p in this equation encompasses both hydrodynamic and acoustic contributions, but only the incompressible Reynolds stresses have been accounted for in the source term. Introducing the definition of the shear stress as a function of the Lighthill tensor and using appropriate Green functions combined with the method of image by Powell (where the plane $x_2 = 0$ is defined as a symmetry plane), the solution for the previous equation in the fluid on or above a rigid planar wall reads:

$$p(\boldsymbol{x},t) = \frac{1}{2\pi}\iiint_V \Big[\frac{\partial^2 \rho_0 (u_i u_j - \overline{u_i u_j})}{\partial y_i \partial y_j}\Big]\frac{\mathrm{d}V(y)}{r} - \frac{1}{2\pi}\iint_S \Big[\frac{\partial \tau_{i2}}{\partial y_i}\Big]\frac{\mathrm{d}S(y)}{r}, \qquad \text{for } i \neq 2 \tag{12}$$

where the brackets denote a function evaluated at retarded time, and the shear stress at the wall is defined as:

$$\tau_{i2} = \mu \frac{\partial u_i}{\partial y_2}\Big|_{y_2=0}, \qquad \text{for } i \neq j$$

It was shown, both from experimental measurements and some theoretical considerations, that the surface integral in Eq.(12) may be neglected compared to the volume integral, at least for the frequency and wave number regimes that we are interested in (see for example Blake [11] for some detailed explanations). Therefore, only the volume integral remains in Eq.(12) as a source term for the fluctuating pressure in the fluid on or above the rigid wall. Note that this formulation for the pressure fluctuations contains both the incident and reflected source effects (as for example in the analysis by Curle presented in section 2.1.b).

The spatial and temporal Fourier transform of the surface pressure fluctuations is now defined as:

$$\hat{p}(\boldsymbol{k},\omega) = \frac{1}{(2\pi)^3}\iiint_{-\infty}^{\infty} p(\boldsymbol{x},t)\mathrm{e}^{-\mathrm{i}(\boldsymbol{k}.\boldsymbol{X}-\omega t)}\mathrm{d}^2\boldsymbol{X}\,\mathrm{d}t$$

where $\boldsymbol{k}=(k_1,k_3)$, $\boldsymbol{X}=(X_1,X_3)$, and $\boldsymbol{x}=(\boldsymbol{X},\bar{x_2})$. Applying this operator to Eq.(12) where the surface integral has been removed, yields after several manipulations to the following result:

$$\hat{p}(\boldsymbol{k},\omega) = \frac{\mathrm{i}}{(2\pi)^2}\iiint_{V} \widetilde{T}_{ij}(\boldsymbol{y},\omega)\Big(\sqrt{k_0^2-k^2}\,\delta_{i2}+k_i\Big)\Big(\sqrt{k_0^2-k^2}\,\delta_{j2}+k_j\Big) \times \frac{\mathrm{e}^{(\mathrm{i}y_2\sqrt{k_0^2-k^2})}}{\sqrt{k_0^2-k^2}}\mathrm{e}^{-\mathrm{i}\boldsymbol{k}.\boldsymbol{y}}\,\mathrm{d}V(\boldsymbol{y}) \quad (13)$$

where $i,j=1,3$ in $k_{i,j}$, and $k=|\boldsymbol{k}|=\sqrt{k_1^2+k_3^2}$. The temporal Fourier transform of the Lighthill tensor $\widetilde{T}_{ij}$ should be understood as:

$$T_{ij}(\boldsymbol{y},t-r/c_0) = \int_{-\infty}^{\infty}\widetilde{T}_{ij}(\boldsymbol{y},\omega))\mathrm{e}^{-\mathrm{i}\omega(t-r/c_0)}\mathrm{d}\omega$$

where $r^2=(x_1-y_1)^2+y_2^2+(x_3-y_3)^2$. Eq. (13) which was first derived by Ffowcs Williams [19] is of particular interest because it describes the generation of surface turbulent pressure fluctuations of various length scales and frequencies by the adjacent turbulent boundary layer flow.

Rewritting the previous equation in term of the Fourier transform of the source density:

$$\widehat{\widetilde{T}_{ij}}(y_2,\boldsymbol{k},\omega) = \frac{1}{2\pi^2}\iint_{-\infty}^{\infty}\widetilde{T_{ij}}(\boldsymbol{y},\omega)\mathrm{e}^{-\mathrm{i}\boldsymbol{k}.\boldsymbol{y}}\mathrm{d}y_1\mathrm{d}y_3$$

gives the final result:

$$\hat{p}(\boldsymbol{k},\omega) = \mathrm{i}\int_0^{\infty}\widehat{\widetilde{T}_{ij}}(y_2,\boldsymbol{k},\omega)\Big(\sqrt{k_0^2-k^2}\,\delta_{i2}+k_i\Big)\Big(\sqrt{k_0^2-k^2}\,\delta_{j2}+k_j\Big) \times \frac{\mathrm{e}^{(\mathrm{i}y_2\sqrt{k_0^2-k^2})}}{\sqrt{k_0^2-k^2}}\,\mathrm{d}V(\boldsymbol{y}) \quad (14)$$

The wave-number frequency spectrum of the wall pressure fluctuations (assumed homogeneous in the y_1-y_3 plane) is related to the modulus of $\hat{p}(\boldsymbol{k},\omega)$ as:

$$\Phi_p(\boldsymbol{k},\omega)\delta(\boldsymbol{k}-\boldsymbol{k}')\delta(\omega-\omega') = <\hat{p}(\boldsymbol{k},\omega)\,\hat{p}(\boldsymbol{k}',\omega')> \quad (15)$$

where the brackets denote the ensemble average.

Mean-Shear Turbulent Interaction In the case of incompressible flow, a particular factorization of the source term in Eq.(11) yields to a result that characterizes the interaction between the mean-shear and the turbulent structures in expressing the surface pressure fluctuations. This expression reads:

$$\hat{p}_{MS}(\boldsymbol{k},\omega) = \mathrm{i}\rho_0\int_0^{\infty}\frac{\partial U_1}{\partial y_2}\frac{k_1\hat{u}_2(y_2,\boldsymbol{k},\omega)}{\sqrt{k_0^2-k^2}}\mathrm{e}^{\mathrm{i}y_2\sqrt{k_0^2-k^2}}\mathrm{d}y_2\,, \qquad \text{for } k>k_0 \quad (16)$$

The remaining contribution of the source term (which is still contained in Eq.(14)) is associated to the so-called turbulence/turbulence interaction. Some theoretical and modelisation works seem to indicate that this contribution is small relatively to the mean-shear turbulence interaction.

Introducing further assumptions on the turbulence behavior, Blake [11] arrives to the following expression for the surface pressure spectrum:

$$\Phi_p(\boldsymbol{k},\omega) = \rho_0^2 U_\tau^4 \frac{k_1^2}{k_1^2+k_3^2} \int_0^\infty L_2(y_2)\, \frac{\overline{u_2^2}}{U_2^2} \left(\frac{1}{U_\tau^2} \frac{\partial U_1}{\partial y_2}(y_2) \right)^2 \Phi_{22}(\boldsymbol{k},y_2) \times \Phi_m(\omega - U_c(y_2)k_1)\, \mathrm{e}^{-2|k|y_2}\, \mathrm{d}y_2 \quad (17)$$

where the newly introduced quantities in this formula are detailed in the next section.

2.6 The TNO Trailing-Edge Noise Model

This model which was originally proposed by Parchen [1] is gathering several from the previous results. These are used to formulate a far field noise level expression as a function of turbulent boundary layer quantities. These data can be collected from any fluid flow solver which includes a description of the turbulent boundary layer. For example, a panel method coupled to an integral boundary layer formulation as in the software XFOIL [20] can be used. Alternatively, any CFD code including a turbulence model for the boundary layer can be considered.

2.6.a Model Formulation

The first part of the model is based on the formula (16) expressing the contribution of the mean-shear/turbulence interaction in the boundary layer and which relates the turbulent boundary layer characteristic data to the fluctuating surface pressure. Using the fact that the wave number-frequency spectrum of the wall pressure fluctuations is related to the modulus of its Fourier transform (Eq.(15)), and manipulating, Parchen [1] arrived to the following result for the wave number-frequency surface pressure spectrum:

$$\Phi_p(\boldsymbol{k},\omega) = 4\rho_0^2 \frac{k_1^2}{k_1^2+k_3^2} \int_0^\infty L_2(y_2)\, \overline{u_2^2} \left(\frac{\partial U_1}{\partial y_2}(y_2) \right)^2 \Phi_{22}(\boldsymbol{k},\omega) \times \Phi_m(\omega - U_c(y_2)k_1)\, \mathrm{e}^{-2|k|y_2}\, \mathrm{d}y_2 \quad (18)$$

where $|k|$ is the norm of the wave number $\boldsymbol{k}=(k_1,0,k_3)$, L_2 is the vertical integral length which characterizes the vertical extent of the turbulent eddies, $\overline{u_2^2}$ is the root mean square (rms) value of the vertical velocity fluctuations, U_1 is the streamwise mean velocity (its derivative, the mean shear, actually appears in the integral), Φ_{22} is the spectrum of the vertical velocity fluctuations (also named the turbulent shear stress), Φ_m is the so-called moving axis spectrum which describes how Φ_{22} is distorted by the generation and destruction of eddies during their convection past the trailing edge, and U_c is the convection velocity of these eddies.

Before relating this wave number-frequency spectrum to the far field noise, the two spectra Φ_{22} and Φ_m present in the previous integral across the boundary layer are analytically given using results from turbulence theory.

The moving axis spectrum is assumed to be gaussian and takes the following form:

$$\Phi_m(\omega - U_c k_1) = \frac{1}{\alpha_{\mathrm{Gauss}}\sqrt{\pi}} \mathrm{e}^{-[(\omega - U_c k_1)/\alpha_{\mathrm{Gauss}}]^2}$$

where the gaussian constant α_{Gauss} is a function of the eddy convection velocity and turbulent length scale:

$$\alpha_{\mathrm{Gauss}} = 0.05\, U_c / L_2$$

The convection velocity is in turn a function of the local boundary layer velocity as:

$$U_c(y_2) = c_\alpha U_1(y_2)$$

where the constant c_α is set equal to 0.7.

The Karman three-dimensional kinetic energy spectrum for isotropic turbulence reads:

$$E(k) = \frac{110\,\Gamma(5/6)}{27\sqrt{\pi}\,\Gamma(1/3)} \frac{k_T}{k_e} \frac{(k/k_e)^4}{[1+(k/k_e)^2]^{17/6}} \tag{19}$$

where k_e is the wave number of energy containing eddies, and k_T the turbulent kinetic energy. From this equation, the energy density spectrum for the vertical fluctuations in the $k_1 - k_3$ plane can be expressed, assuming again isotropy, as:

$$\Phi_{22}(k_1, k_3) = \frac{4}{9\pi k_e^2} \frac{(k_1/k_e)^2 + (k_3/k_e)^2}{[1+(k_1/k_e)^2 + (k_3/k_e)^2]^{7/3}} \tag{20}$$

The second part of the model consists in expressing the far field noise as a function of the previous wave number-frequency of the surface pressure fluctuations defined by Eq.(18). Using the results of Chase [17] and Brooks and Hodgson [10] (see Eq.(10)), the far field pressure spectrum density can be expressed as an integral of the wall pressure spectrum over the wave number component in the flow direction:

$$S(\omega) = \frac{L}{4\pi R^2} \int_{-\infty}^{\infty} \frac{\omega}{c_0 k_1} \Phi_p(\boldsymbol{k}, \omega)|_{k_3=0}\, \mathrm{d}k_1 \tag{21}$$

where R denotes the distance of the observer to the trailing edge, and L the span extent of the trailing edge.

At this point, the integral length L_2, the mean shear $\partial U_1/\partial y_2$, the wave number k_e, and the turbulent shear stress $\overline{u_2^2}$ still need to be specified in order to close the model. The specification of these quantities depends on the methodology that is used to calculate the flow field. Two approaches are considered: the integral boundary layer panel code XFOIL [20], and a Reynolds-Average Navier-Stokes solver (in our case EllipSys2D [21, 22, 23]).

2.6.b Model Based on Integral Boundary Layer Method

In the case of a XFOIL calculation, boundary layer equations are solved in order to determine its development along the airfoil chord. This calculation is coupled to a panel method used to compute the inviscid flow outside the boundary layer. The data of interest that are given as an output from XFOIL are: the skin friction coefficient at the wall C_f, the momentum thickness θ, the displacement thickness δ^*, the velocity at the edge of the boundary layer U_0.

The missing data needed for the model proposed in the previous section are obtained using results from classical turbulent boundary layer theory, as well as isotropic turbulence.

The boundary layer thickness δ can be related to the momentum thickness and the displacement thickness by using the relation by Drela and Giles:

$$\delta = \theta\left(3.15 + \frac{1.72}{H_k - 1}\right) + \delta^*$$

where $H_k = \delta^*/\theta$ is the kinematic shape factor which is also given as an output of XFOIL. The velocity profile can then be approximated in the boundary layer by using Cole's law of the wall/law of the wake [24] as:

$$U_1(y_2) = u^*\left(\frac{1}{\kappa}\ln\left(\frac{u^* y_2}{\nu}\right) + B + \frac{1}{2}W\left(\frac{U_0}{u^*} - \frac{1}{\kappa}\ln\left(\frac{u^*\delta}{\nu}\right) - B\right)\right)$$

where $\kappa = 0.41$ is the Karman constant, $B = 5.5$, and $u^* = U_0\sqrt{C_f/2}$ is the friction velocity. The wake function is defined as:

$$W = 1 - \cos(\pi y_2/\delta)$$

The velocity profile formula can easily be derived to obtain the mean shear.

The next quantity to be defined is the integral length scale L_2. In a first step, the mixing length scale expression proposed by Schlichting [25] is used:

$$l_m = 0.085\,\delta \tanh\left(\frac{\kappa y_2}{0.085\,\delta}\right)$$

Then, the integral length is approximated as:

$$L_2 = \frac{l_m}{\kappa} \tag{22}$$

In the case of isotropic turbulence (such an assumption is here needed in order to get the following approximation), the integral length is well defined and related to the wave number of the energy-bearing eddies as:

$$L_2 = \frac{\sqrt{\pi}\,\Gamma(5/6)}{\Gamma(1/3)}\frac{1}{k_e} \tag{23}$$

yielding:

$$k_e \approx 0.7468/L_2$$

which can be used for evaluating the normal velocity fluctuations spectrum Φ_{22} in Eq.(20).

The last quantity to be defined is the turbulent shear stress. Prandtl's mixing length hypothesis assumes that the turbulent viscosity ν_t is related to the mixing length and the mean shear as:

$$\nu_t = l_m^2\left|\frac{\partial U_1}{\partial y_2}\right|$$

Then, the turbulent kinetic energy k_T is given by:

$$k_T = \sqrt{\nu_t\left(\frac{\partial U_1}{\partial y_2}\right)^2/C_\mu} \tag{24}$$

where $C_\mu = 0.09$. The turbulent shear stress is then assumed proportional to the turbulent kinetic energy as:

$$\overline{u_2^2} = \alpha k_T \tag{25}$$

where the constant $\alpha = 0.45$ on the suction side, and $\alpha = 0.3$ on the pressure side of an airfoil.

2.6.c Model Based on RANS Solution

In the case of a RANS code is used, many of the previous model input data are directly accessible from the computed quantities. In particular, the velocity profile, and thereby the mean shear, accross the boundary layer can be extracted from the velocity field at the trailing edge. Similarly, the turbulent kinetic energy k_T (as well as its dissipation rate ϵ) can be interpolated along the same boundary layer path. Eq.(25) is then used to obtain the turbulent shear stress $\overline{u_2^2}$.

The integral length scale is the last remaining quantity to be defined. Wagner *et al* [26] used the simple assumption that the vertical correlation length is proportional to the mixing length scale as in Eq.(22).

Lutz *et al* [27] argues that the determination of the vertical length scale is most crucial for the consistency of the noise prediction. Therefore, a more elaborate

approach to evaluate L_2 is proposed. In the case of isotropic turbulence, the integral length is well defined as a function of the wave number of the energy-bearing eddies as:

$$L_2 = \frac{\sqrt{\pi}\,\Gamma(5/6)}{\Gamma(1/3)}\frac{1}{k_e}$$

The Kolmogorov spectrum in the inertial subrange reads:

$$E(k) = C\frac{\epsilon^{2/3}}{k_T^{5/3}}$$

where the constant $C \approx 1.5$ was experimentally determined, and ϵ is the turbulent energy dissipation rate. By comparing the previous spectrum with the asymptotic behavior of the Karman spectrum in Eq.(19), the wave number of the energy bearing eddies k_e can be deduced:

$$k_e \approx 1.9275\frac{\epsilon}{k_T^{3/2}}$$

Combining this equation with the above equation relating the wave number k_e and the integral length L_2 in the case of isotropic turbulence, the following result can be established:

$$L_2 \approx 0.387\frac{k_T^{3/2}}{\epsilon} \tag{26}$$

This latter approach will be used in the following noise calculations based on RANS computational results (instead of using Eq.(22)).

Note that in the original model proposed by Parchen [1], an alternative approximation for the vertical integral length scale that can be employed in conjunction with a Reynolds-Averaged Navier-Stokes solution method was proposed. The mixing length is first approximated by:

$$l_m = \frac{C_\mu^{3/4} k_T^{3/2}}{\epsilon}$$

Then, combining with Eq.(22) relating the mixing length scale to the integral length scale, this yields:

$$L_2 \approx 0.401\frac{k_T^{3/2}}{\epsilon}$$

which is very similar to Eq.(26).

3 Evaluation of the TNO model

3.1 VTE-kav Airfoil

In order to validate our implementation of the TNO model, it will be applied to the VTE-kav airfoil that was designed by Würz at IAG (Institute für Aerodynamik und Gasdynamik der Universität Stuttgart). This airfoil was acoustically measured in the laminar wind tunnel at IAG by Herrig *et al* [28]. The airfoil has a chord $C = 0.8$ m, a span of 1 m, the inflow velocity was set to $U_\infty = 60$ m/s resulting in a Reynolds number approximately equal to $Re = 3.1 \times 10^6$ and a Mach number $M_0 = 0.178$. The angle of attack of the airfoil relatively to the inflow is 2.7^o. The data from the microphones used to record the noise were post-processed so that the resulting Sound Pressure Levels are given at 1 m from the airfoil trailing edge.

In a numerical study conducted by Humpf [29], the previous experimental results are compared to semi-empirical acoustic models including the so-called BPM model [3], as well as the TNO model. These models have been implemented within the noise prediction tool NAFNoise, developed by Moriarty and Migliore [30], which was used for this numerical study. In addition, the commercial code FLUENT which is equipped with its own aeroacoustic models was also used.

The previous references are compared to numerical calculations that were performed as part of the present work. As exposed in the first part of this report, the integral boundary layer code XFOIL and the in-house Navier-Stokes solver EllipSys2D are used to compute the fluid flow. Acoustic calculations are performed by using the results of these two codes as an input for the TNO model.

In Figures 5(a) and (b), the boundary layer thickness δ normalized by the chord length and the skin friction coefficient C_f along the airfoil chord are displayed. There is a general good agreement between all results. As far as noise modeling is concerned (if using TNO model at least), the quantities of interest are located at, or just upstream the trailing edge. There, the XFOIL calculations seems to slightly overestimate the boundary layer thickness, and the EllipSys2D calculations overestimates the friction coefficient though a value identical to the experimental one is recovered when approaching the trailing edge due to an abrupt drop of this coefficient on the very last section of the airfoil chord.

Figs.6(a-c) display profiles across the boundary layer at the trailing edge and on the suction side for the following quantities respectively: tangential velocity (normalized with the fluid velocity at the edge of the BL), the mean shear, the turbulent kinetic energy (normalized by the squared free-stream velocity), and the integral length scale (of the vertical velocity fluctuations). Note that the latter quantity is given by Eq.(22) if using XFOIL, and Eq.(26) if using EllipSys2D. There is a good agreement between all normalized tangential velocity profiles. The turbulent kinetic energy is significantly underestimated by the EllipSys2D (and in a lesser degree by Fluent) calculations, whereas XFOIL result approximated with Eq.(24) is relatively close to the experimental measurements in the outer part of the boundary layer.

The far field Sound Pressure Levels (SPL) calculated by the TNO model, both using XFOIL or EllipSys2D, produce very similar results, but seriously underestimate the experimental measurements as shown in Fig.7. An identical discrepancy was also observed with the NAFNoise code in the calculations performed by Humpf [29] (which was expected as our implementation of the TNO model together with the XFOIL code should be nearly indentical as the one in NAFNoise). It is interesting to note here that the simplified semi-empirical trailing edge noise model by Brooks, Pope and Marcolini [3] is performing much better in this case, and produces results in good agreement with the measurements (see Humpf [29]).

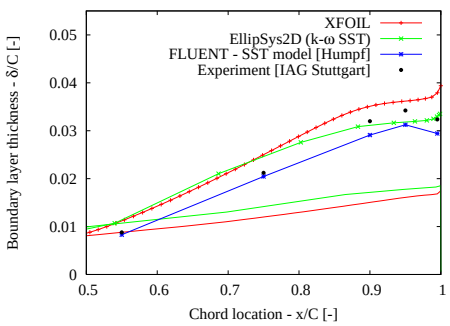

(a) Boundary layer thickness

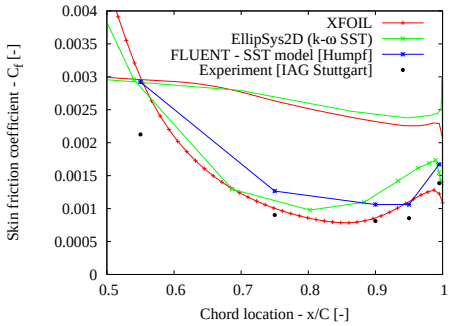

(b) Skin friction coefficient

Figure 5. Boundary Layer Characteristics
(Lines with points: Suction side; Lines without points: Pressure side)

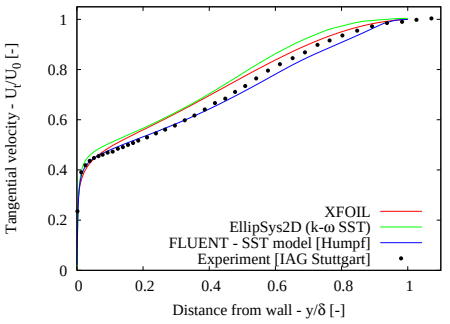

(a) Velocity profile

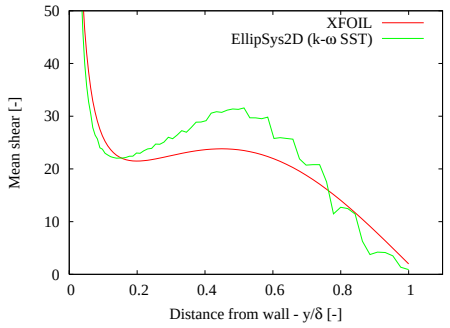

(b) Mean shear

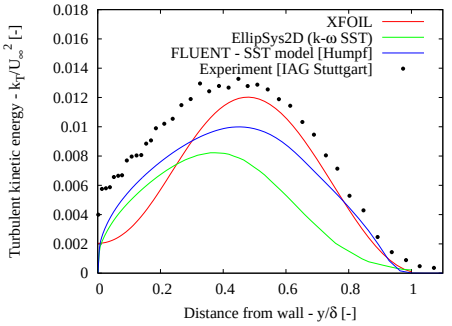

(c) Turbulent kinetic energy

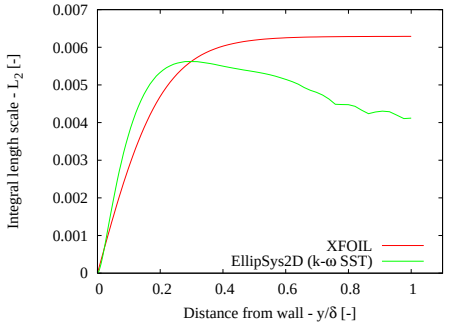

(d) Integral length scale

Figure 6. Boundary Layer Profiles at Trailing Edge (Suction side - $x/C = 0.995$)

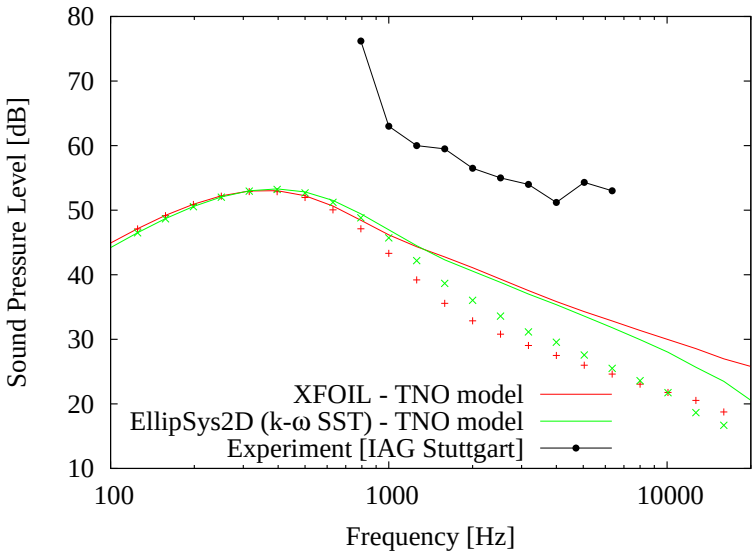

Figure 7. Sound Pressure Levels (Points: TNO model for suction side only)

3.2 Comparison with CAA Results

In this section, results from the TNO model are compared to those obtained with a Computational Aero-Acoustics (CAA) approach. Such calculations were performed at MEK/DTU on the NACA-0015 airfoil by Zhu [31] and are used for this comparison. The CAA algorithm, based on a splitting of the flow into an incompressible and an inviscid acoustic part, was developed by Shen and Sørensen [32, 33]. The incompressible equations are solved using a Large Eddy Simulation (LES) technique for simulating the turbulent flow. The turbulent vortices smaller than the numerical grid size are modelled using a Sub-Grid Scale model. To reduce the computational time, the Reynolds number chosen for the considered test-case is relatively low: $Re = 10^5$. The Mach number is set to $M = 0.2$. For standard atmospheric air conditions at room temperature, this corresponds to an inflow velocity $U_\infty \approx 68.6$ m/s, and an airfoil chord $C \approx 0.022$ m. The angle of attack of the flow is set to $\alpha = 5^o$ for the CAA calculations.

We are interested in evaluating the TNO with input data originating from the incompressible part (LES calculation) of the CAA solver. However, results for this calculation are only available for an angle of attack equal to $\alpha = 4^o$. Note that these LES and CAA calculations were performed in a two-dimensional configuration, and it should therefore be expected that the turbulent eddies are larger in size (than in an actual 3D flow field) since they are not subject to 3D instabilities.

The TNO model calculation will involve results with input data originating both from the XFOIL code and the RANS solver EllipSys2D as described earlier. As mentioned above, the TNO model will also be fitted with input data originating from a LES calculation. From this unsteady calculation, the following time-averaged data are extracted near the trailing edge: boundary layer thickness δ, friction coefficient C_f, velocity profile across the boundary layer $U_1(y_2)$ (from which the mean shear $\partial U_1/\partial y_2$ is deduced), and the turbulent kinetic energy k_T across the boundary layer. To complete the model input data, the integral length scale is still needed. Eq.(22) will be used together with the Schlichting approximation for the mixing length scale.

The boundary layer thickness and the skin friction coefficient along the airfoil surface are displayed in Figs.8(a-b). It should first be noted that the EllipSys2D and the LES calculations both predict a trailing edge separation on the suction side, whereas the XFOIL code doesn't. It does also explain the curious sudden high values of the boundary layer thickness for the EllipSys2D calculations in the vicinity of the detachment point on the suction side, and on the pressure side where the boundary layer is about to detach as seen on the skin friction, which are due to a convergence failure of the algorighm used to determine the boundary layer thickness in this region. Nethertheless, the skin friction coefficients on both sides of the airfoil near the trailing edge predicted by LES and RANS methods match perfectly. As for the boundary layer thickness, it can be seen that the LES calculation predict a much thicker boundary layer on the suction side. Velocity profiles and mean shear somehow differ from each other for all methods as seen in Figs.9(a-b). RANS and XFOIL calculations predict similar turbulent kinetic energy and integral length scale across the boundary layer, but the LES calculation predicts noticeably higher values. As for the turbulent energy, this is due to the different nature (and probably better quality as it will be seen in the acoustic results) of the LES turbulence modelling. As for the integral length scale, this is a direct consequence of the prediction of a thicker boundary layer. Sound Pressure Levels at a distance of $R = 5C \approx 0.11$ m obtained with the TNO model and from the CAA computation are reported in Fig.10. It can be seen that the TNO model results fitted with the LES input data show the closest agreement with the CAA results. The latter can be taken as a reference since it is a numerical model

involving much less physical assumptions compared to the TNO model. The model fitted with RANS data predicts lower SPL, but the peak sound frequency is well predicted. The XFOIL calculation provides the poorest results. It must be noted that the TNO model fitted with LES input data uses data obtained at an angle of attack $\alpha = 4^o$. It could therefore be expected that input data obtained for an angle of attack $\alpha = 5^o$ would produce slightly higher SPL, and thereby get closer to the CAA results.

It can be concluded that some of the deficiencies of the TNO model probably partly originates from the quality of the input data. In particular, as shown in this test-case too small turbulent kinetic energy and a too thin boundary layer thickness are the main reasons for the lower performance of the TNO model with standard inputs (RANS and XFOIL) compared to the LES input data. However, it remains unclear whether the TNO model fitted with LES input data fails to match the CAA calculation because of the crude approximation of the integral length scale, or because of a deficiency inherent to the TNO model formulation itself. A possible cause for this discrepency is the existence of vortices generated in the turbulent boundary layer on the suction side of the airfoil in the LES calculation (see Zhu [31]). These vortices are convected downstream along the airfoil chord and shed in the wake. In the CAA calculation, these vortices will act as noise sources during their convection along the chord and radiate in the far field. Such a mechanism is not taken into account in the TNO model. It would therefore be interesting to evaluate the importance of this previous mechanism relatively to the trailing edge noise, in order to estimate its relative contribution to the overall far field noise predicted by the CAA code.

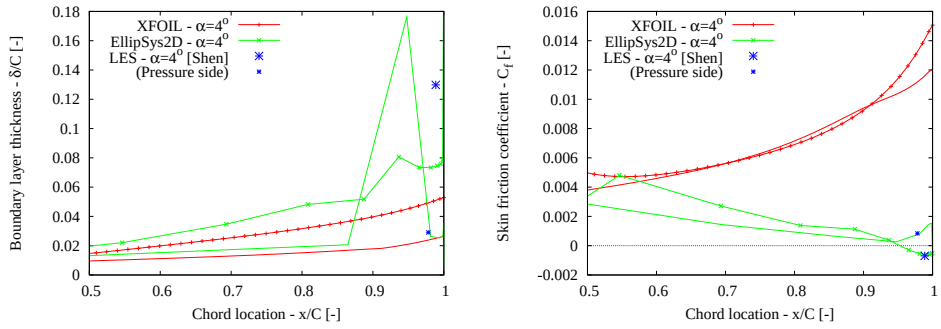

(a) Boundary layer thickness

(b) Skin friction coefficient

Figure 8. Boundary Layer Characteristics
(Lines with points: Suction side; Lines without points: Pressure side)

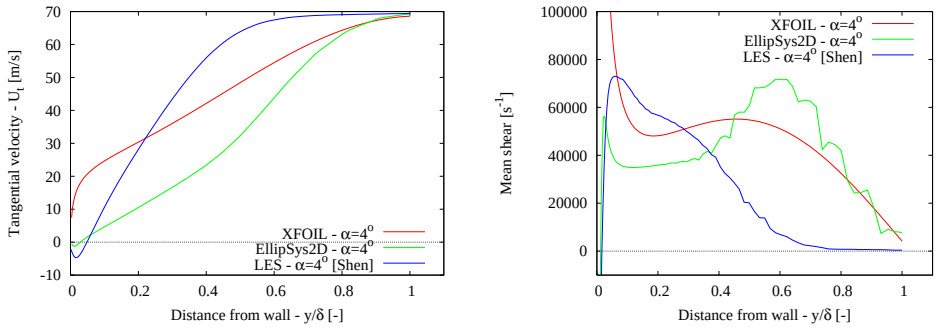

(a) Velocity profile

(b) Mean shear

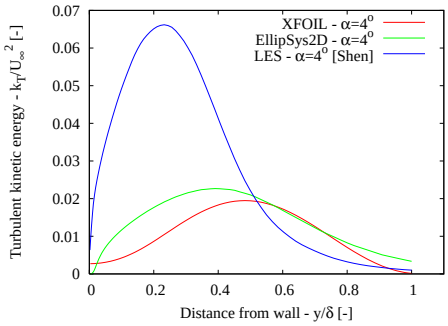

(c) Turbulent kinetic energy

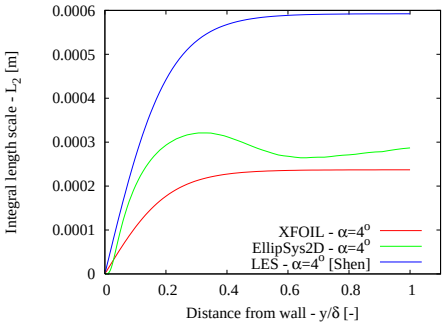

(d) Integral length scale

Figure 9. Boundary Layer Profiles at Trailing Edge (Suction side - $x/C = 0.995$)

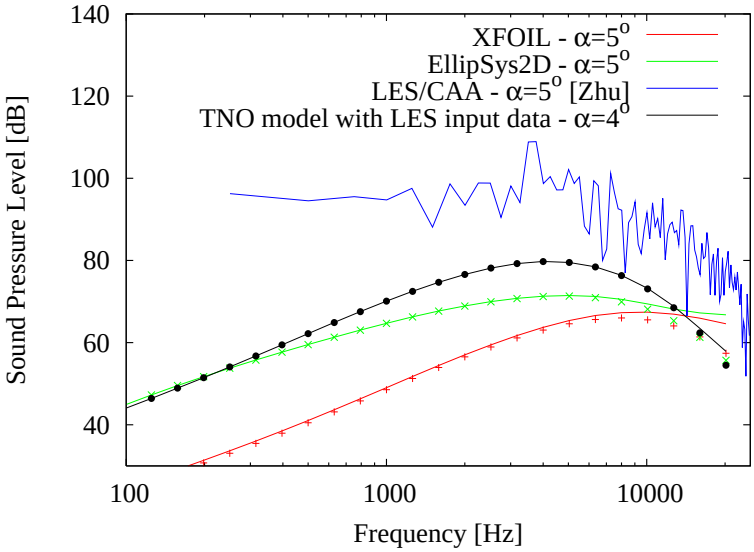

Figure 10. Sound Pressure Levels (Points: TNO model for suction side only)

3.3 Various Airfoils Comparison

In this section, a collection of wind turbine airfoils are studied with respect to their trailing edge induced noise. Both two-dimensional Navier-Stokes computations with EllipSys2D, as well as results obtained with XFOIL are considered. The goal is two-sided. Firstly, we are interested in analyzing the TNO in more details and evaluating the influence of the airfoil shape onto the radiated trailing edge noise. Secondly, differences between the use of the model fed with boundary layer data from XFOIL or from the RANS code are investigated. The following airfoil profiles are investigated: NACA-0012, NACA-63415, RISØ-B1-18, S809, and S822. For all calculations in this section, the Reynolds number is set equal to $Re = 1.1 \times 10^6$.

Comparison at Constant C_l In the first part of this comparison analysis, calculations are performed at various angles of attack (depending on the considered airfoil) such that the resulting lift coefficient is identical for all airfoils, and equal to $C_l = 0.6$. Note that in all these calculations, transition was set free by using the e^n-model implemented in the EllipSys2D code, and that the same transition location was enforced in the XFOIL calculations.

The evolutions of the boundary layer thickness and of the skin friction coefficient along the airfoil chord on the suction side are reported in Figs.11 and 12, respectively. It can be seen that both Navier-Stokes and XFOIL calculations predict the same tendencies regarding the impact of the airfoil geometries on these quantities. It should be noted that the flow on the suction side of the S809 airfoil separates locally around the mid-chord, but reattaches afterward due to the transition to turbulence that occurs in the recirculation bubble.

Velocity and mean shear profiles across the boundary layer in the vicinity of the trailing edge are reported in Figs.13 and 14, respectively. The shapes of these profiles slightly differ between the CFD and XFOIL calculations. The S822 presents the highest mean shear (in particular for the XFOIL calculation). This yields to an significantly higher turbulent kinetic energy across the boundary layer as observed in Fig.15.

Fig.16 displays the integral length scale. It can be seen that XFOIL calculation predicts a higher value for the NACA-0012 airfoil, and EllipSys2D for the S809 airfoil.

These previous results are illustrated in the Sound Pressure Levels obtained from the TNO model which is using the previous data (see Fig.17). Indeed, the XFOIL calculations predict that the S822 produces the highest SPL of all the considered airfoils. If only suction side generated noise is considered, EllipSys2D calculations predict S809 as the noisiest airfoil. Note that the NACA-0012 presents a very high pressure side generated noise for the EllipSys2D calculation (this increase in noise level can also be observed to a lesser extent in the XFOIL calculation at higher frequency $f \approx 10000\,\mathrm{Hz}$), which is most probably non-physical due to a laminar separation located near the trailing edge of the airfoil. Remind that the TNO model is in principle not valid for detached flows. In both XFOIL and EllipSys2D calculations, NACA-63415 and RISØ-B1-18 are the airfoils that produce less noise. This might be explained by a combination of low integral length scale and turbulent kinetic energy across the boundary layer.

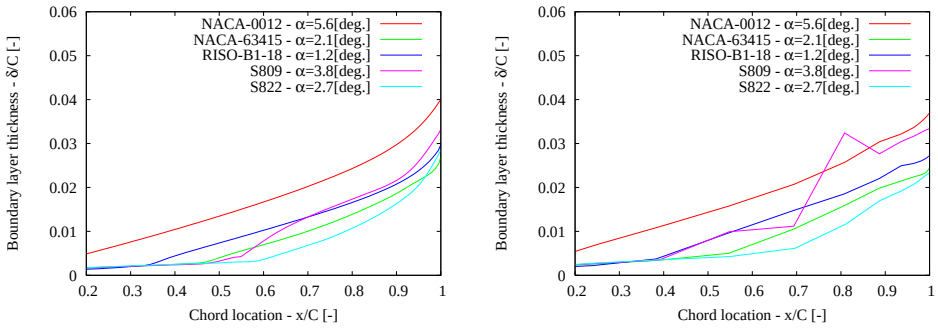

(a) XFOIL (b) EllipSys2D

Figure 11. Boundary Layer Thickness (Suction side)

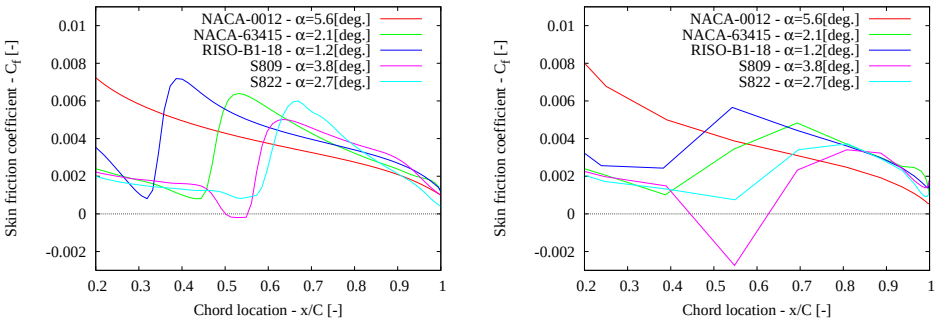

(a) XFOIL (b) EllipSys2D

Figure 12. Skin Friction Coefficient (Suction side)

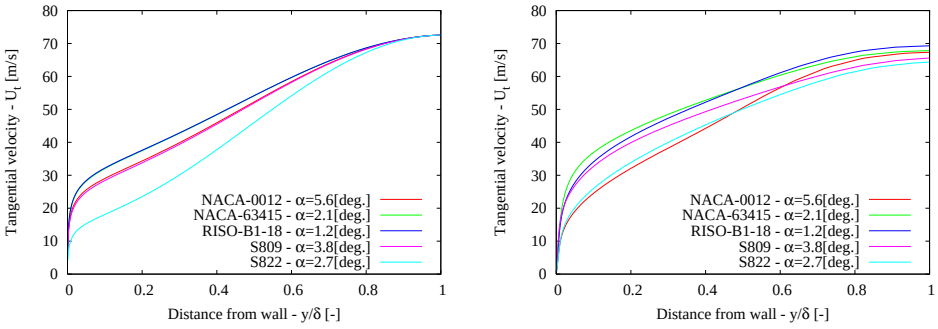

(a) XFOIL (b) EllipSys2D

Figure 13. Velocity Profile at Trailing Edge (Suction side - $x/C = 0.995$)

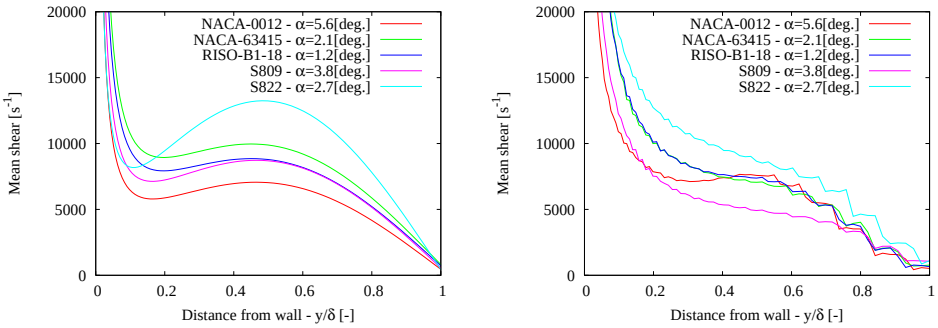

(a) XFOIL (b) EllipSys2D

Figure 14. Mean Shear Profile at Trailing Edge (Suction side - $x/C = 0.995$)

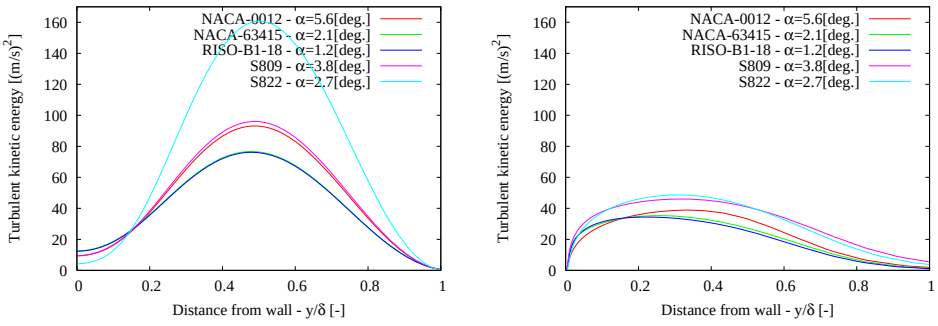

(a) XFOIL (b) EllipSys2D

Figure 15. Turbulent Kinetic Energy Profile at TE (Suction side - $x/C = 0.995$)

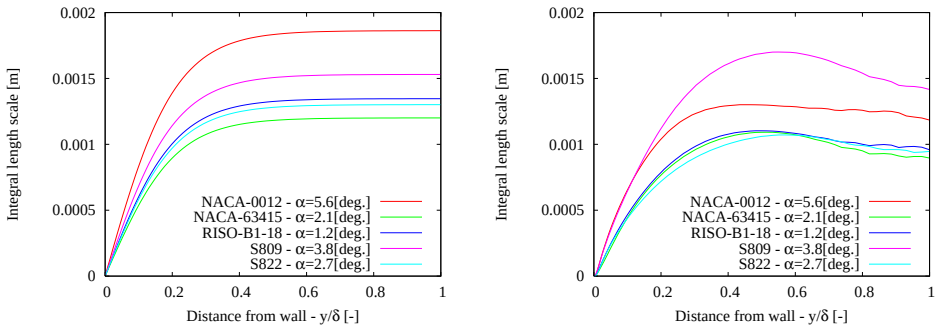

(a) XFOIL (b) EllipSys2D

Figure 16. Integral Length Scale Profile at TE (Suction side - $x/C = 0.995$)

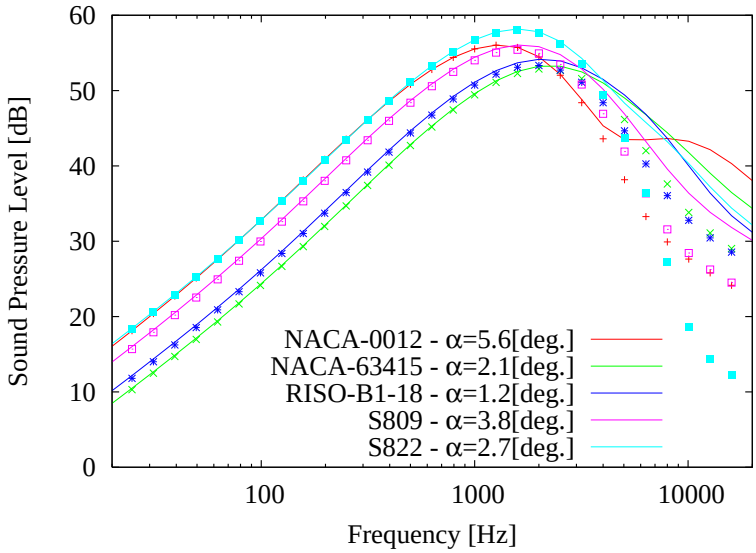

(a) XFOIL

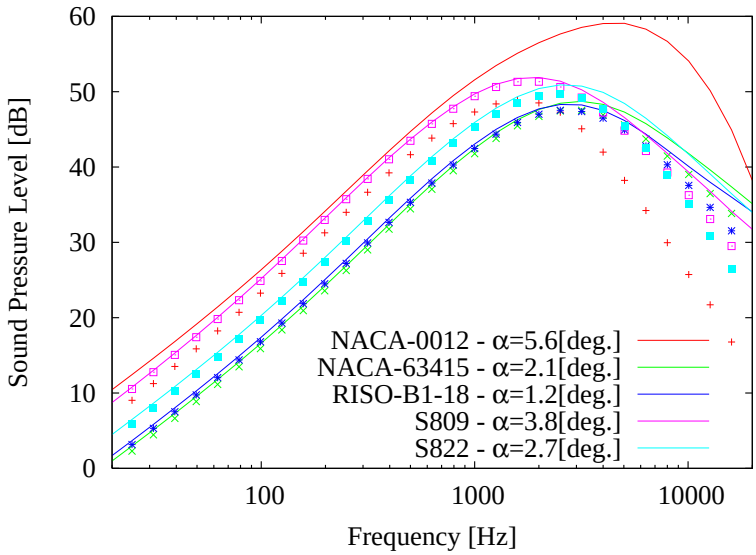

(b) EllipSys2D

Figure 17. Sound Pressure Levels (Points: TNO model for suction side only)

Comparison at Constant Angle of Attack In the second part of this comparison analysis, the calculations are performed at two given angles of attack: $\alpha = 0$ and 3^o, all with fixed transition location enforced at $x/C = 5\%$ on both the suction and the pressure sides of the airfoils. Only three of the airfoils considered previously are retained: NACA-63415, RISØ-B1-18, and S809. The results are reported in Fig.18 to 24.

A first noticeable results is the fact that trailing edge noise level increase with increasing angle of attack, which is expected as the suction side is the main source of noise.

Results are more homogeneous from one airfoil to the other, than for those oberved above for a constant lift. The NACA-63415 and S809 airfoils have very similar noise levels if the input data originate from the same flow solver. However, noise predicted with the XFOIL calculations is noticeably higher than with EllipSys2D. The S809 airfoil produces higher sound levels than the two other airfoils.

If flow calculation methods are compared, it is clear that XFOIL calculations predict higher turbulent kinetic energy and integral length scales across the boundary layer than EllipSys2D. Note however that in some cases, these quantities are dependent on the TNO-model and related assumed formulae, and not only on the calculation method itself. Accordingly, the resulting sound levels are higher.

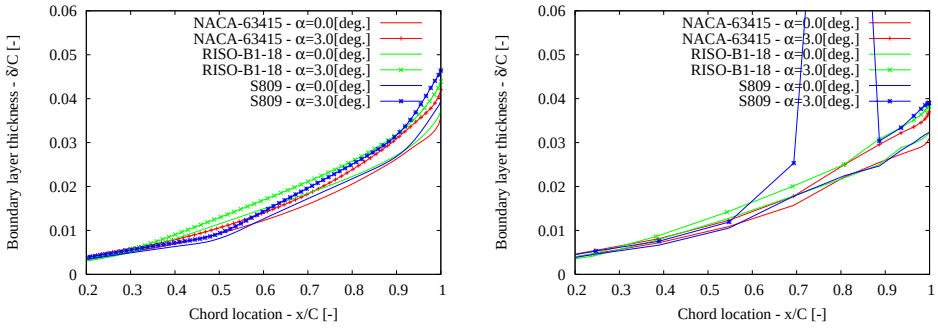

(a) XFOIL (b) EllipSys2D

Figure 18. Boundary Layer Thickness (Suction side)

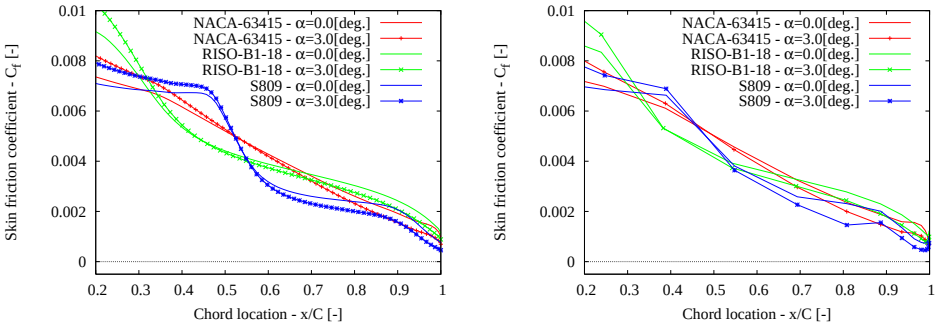

(a) XFOIL (b) EllipSys2D

Figure 19. Skin Friction Coefficient (Suction side)

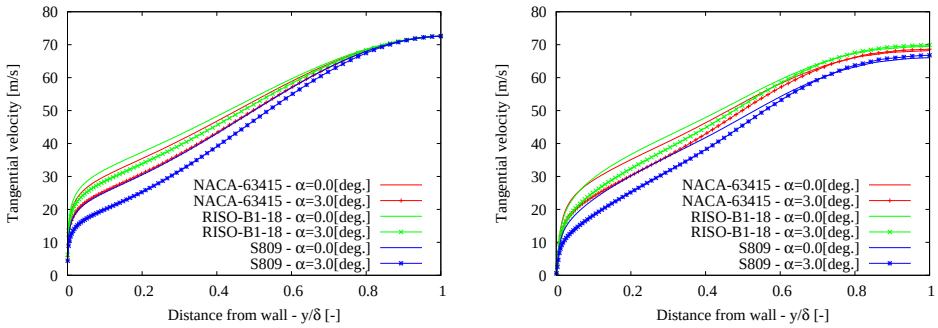

(a) XFOIL (b) EllipSys2D

Figure 20. Velocity Profile at Trailing Edge (Suction side - $x/C = 0.995$)

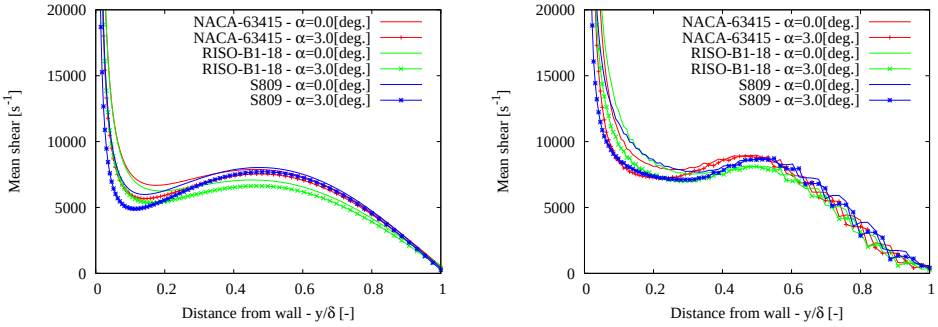

(a) XFOIL (b) EllipSys2D

Figure 21. Mean Shear Profile at Trailing Edge (Suction side - $x/C = 0.995$)

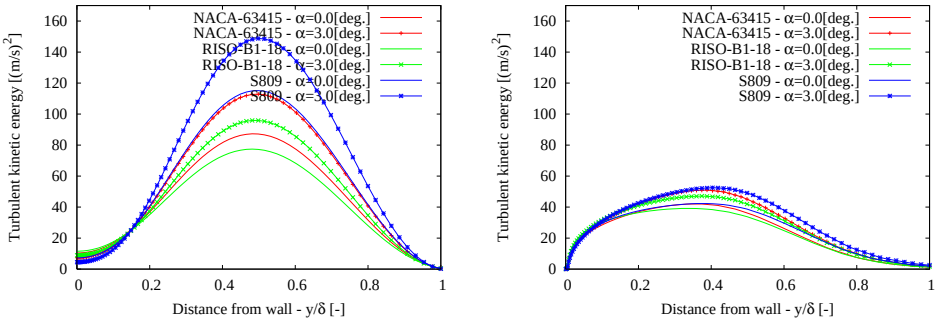

(a) XFOIL (b) EllipSys2D

Figure 22. Turbulent Kinetic Energy Profile at TE (Suction side - $x/C = 0.995$)

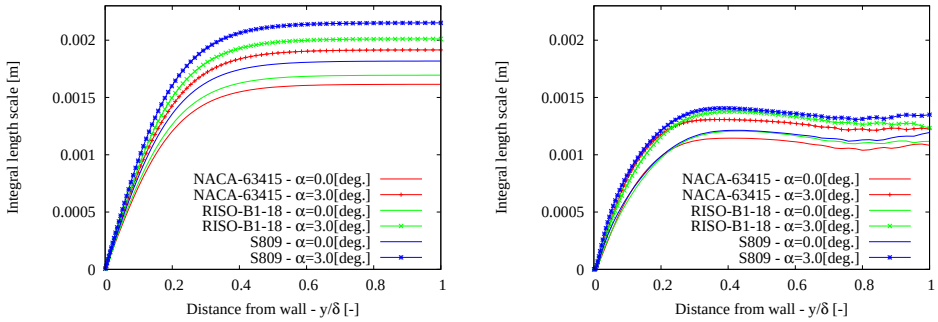

(a) XFOIL (b) EllipSys2D

Figure 23. Integral Length Scale Profile at TE (Suction side - $x/C = 0.995$)

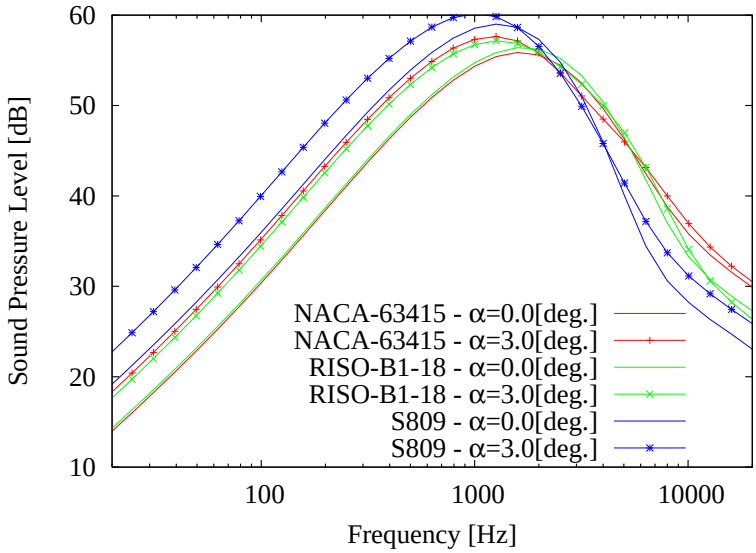

(a) XFOIL

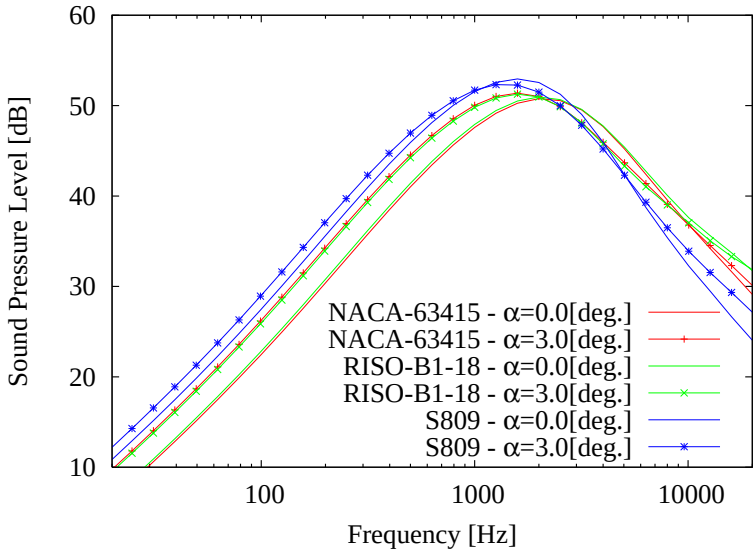

(b) EllipSys2D

Figure 24. Sound Pressure Levels

4 Design of Noise-Optimized Airfoils

In this section, the TNO model is implemented into an optimization program that is originally used for airfoil design. Our goal is now to improve the acoustic properties of given airfoils.

4.1 The Optimization Program *AirfoilOpt*

The optimization code *AirfoilOpt* is an airfoil/blade section profile design tool that was developed at Risø National Laboratory [34, 35]. It is based on a so-called Sequential Linear Programming technique to reduce a given cost function. In short, from a given set of design parameters, at each iteration of the numerical procedure the code calculates the local gradients of the cost function associated to each parameter in order to find a new iterate improving the value of the cost function. This cost function can be a linear combination of various aerodynamic characteristics (such as lift, drag, moment coefficients, lift/drag ratio, transition location, etc...) of the airfoil section. These aerodynamic data are computed with the airfoil analysis code XFOIL by Drela [20]. It is based on a boundary layer integral solution procedure combined with an inviscid panel method. In addition, non-linear constraints on the aerodynamic properties of the airfoil, as well as on its geometry, can be enforced in the optimization process.

As part of the present work, the original optimization code has been extended by introducing the noise level as a possible component of the cost function (see section 2.6.b). In the following calculations, the maximum value of the A-weighted far field noise spectrum across all frequency range will be considered when noise level is introduced in the cost function. Both the pressure and the suction side noise spectrum are considered and are added to each other. However, it turns out that only the suction side generated noise will be of interest for the flow conditions that we are interested in.

In the following of this section, two reference airfoils will be considered and our goal is to further optimize these with respect to their noise level: RISØ-B1-18 and S809. The optimization cost function will only consist of the maximum value of the A-weighted Sound Pressure Level at a given angle of attack. Indeed, it was found difficult to optimize the airfoil noise generation if other aerodynamic quantities were included in the cost function. However, in order to preserve at least some of the aerodynamic properties of the reference airfoils, constraints on the aerodynamic quantities will be enforced during the optimization process.

It must be noted that for each optimization calculation, the iterative procedure is restarted from the original reference airfoil. All calculations are pursued until a local optimum for the cost function is found.

4.2 Airfoil Design - Reference Airfoil: RISØ-B1-18

The first airfoil that is considered is the RISØ-B1-18 airfoil. Its detailed design criteria can be found in Fuglsang and Bak [35]. In few words, it was designed to be transition insensitive, together with a relatively high maximum lift and a smooth stall. It was designed as well to optimize the driving force C_t at operational conditions, i.e. for angles of attack equal to $\alpha = 5.1$ and 10.1^o. Actually, relative angles of attack $\alpha_r = 9$ and 14^o are used in the design algorithm, where $\alpha_r = \alpha - \alpha_0$. For the RISØ-B1-18 airfoil, the angle of attack at zero-lift is $\alpha_0 = -3.9^o$.

As mentioned above, the cost function used in our optimization calculations involves only the maximum value of the A-weighted Sound Pressure Level for a relative angle of attack equal to $\alpha_r = 10^o$ (which corresponds approximately to an actual angle of attack $\alpha = 6.1^o$). The different sets of constraints used to generate the different noise-optimized airfoils are designated as follows:

- **O0**
  Suction side: $y''(0.4 < x/C < 0.9) < -0.15$
  Pressure side: $+0.0 < y''(0.0 < x/C < 0.2)$
  Pressure side: $-1.1 < y''(0.7 < x/C < 0.9)$

  Suction side: $x_{tr}(\alpha_r = 15^o)/C < 0.06$

  $1.77 < C_l(\alpha_r = 17^o) < 1.9$
  $1.50 < C_l(\alpha_r = 26^o) < 1.9$

  $0.075 < C_t(\alpha_r = 9^o)$
  $0.250 < C_t(\alpha_r = 14^o)$
- **O1** Same as O0 but no constraints on C_l, and constraint on C_t is:
  $0.46 < C_t(\alpha_r = 26^o)$
- **O2** Same as O0 but constraints on C_l are:
  $1.77 < C_l(\alpha_r = 17^o) < 2.2$
  $1.30 < C_l(\alpha_r = 26^o) < 1.9$
- **O3** Same as O2 but:
  Suction side: $y''(0.4 < x/C < 0.9) < -0.11$
  Pressure side: $+0.0 < y''(0.0 < x/C < 0.2)$
  Pressure side: $-1.4 < y''(0.7 < x/C < 0.9)$
- **O4** Same as O2 but:
  Suction side: $y''(0.4 < x/C < 0.9) < -0.0$
  Pressure side: $+0.0 < y''(0.0 < x/C < 0.2)$
  Pressure side: $-1.9 < y''(0.7 < x/C < 0.9)$

The quantity y'' denotes the second order derivative of the airfoil shape coordinate in the direction normal to the airfoil chord with respect to the airfoil chord direction, and x_{tr} denotes the transition location, here obtained with the e^n transition model implemented in XFOIL ($n = 9$). All the above constraints involving the lift and tangential force coefficients are enforced in the fully turbulent calculation cases only. In addition, a few geometrical constraints are enforced so that the trailing edge thickness doesn't collapse.

Fig.25 shows the different deviations from the original RISØ-B1-18 profile obtained after convergence of the optimization procedure with the different optimization constraints presented above (The actual profiles are not shown here because the RISØ-B1-18 airfoil coordinates are protected for commercial license purpose). The different input data corresponding to each design and extracted from XFOIL are shown in Figs.26-27. The far field SPLs are plotted on Figs.28(a-b), tangential and lift coefficients as a function of the relative angle of attack on Figs.29(a-b).

As it can be seen on the geometry of the resulting airfoils, relaxing the constraints on the geometry (as done for design O3 and O4) yields to a different general shape of profiles with a higher curvature at the front of the airfoil. The design O4 is actually yielding to the best aeroacoustic properties (in term of maximum A-weighted SPL), closely followed by the design O2. However, the latter one has its peak frequency slightly shifted to a higher value than the former one. All

in all, the gain obtained in term of A-weighted SPL is relatively low (in the order of 1 dB). The gain is slightly more substantial if the non-filtered SPL are considered (in the order of 3 dB). However, it should be noted that it is believed that the RISØ-B1-18 airfoil (in its original configuration) is a relatively silent airfoil. Therefore, it might be difficult for the optimization algorithm to further reduce its noise signature.

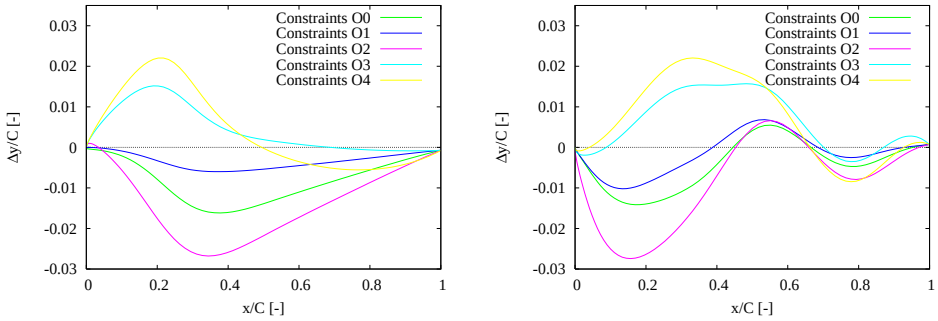

(a) Suction side (b) Pressure side

Figure 25. Optimized Airfoil Shape Deviations from RISØ-B1-18

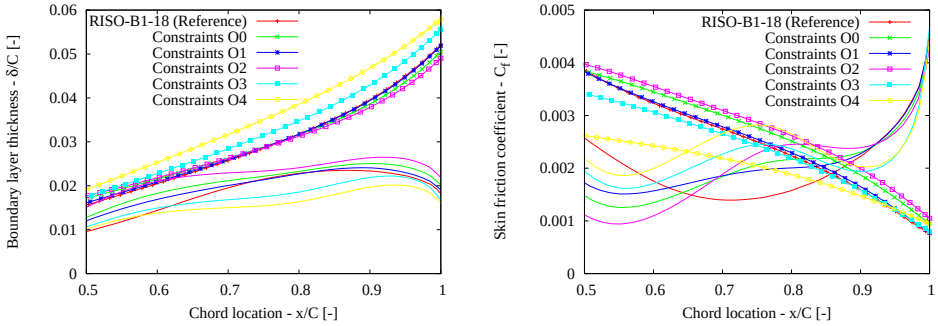

(a) Boundary layer thickness (b) Skin friction coefficient

Figure 26. Boundary Layer Characteristics
(Lines with points: Suction side; Lines without points: Pressure side)

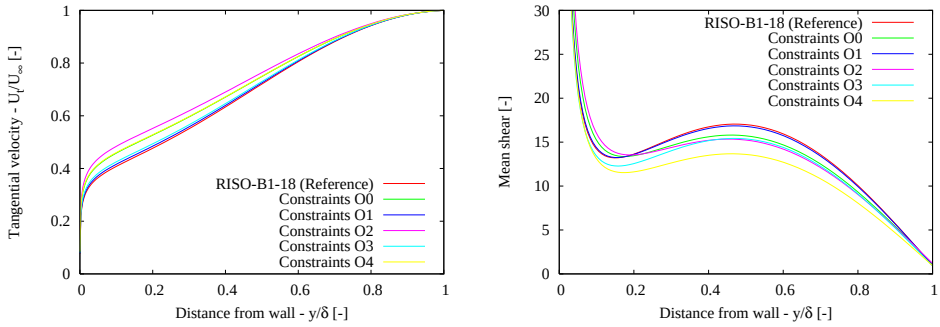

(a) Velocity profile

(b) Mean shear

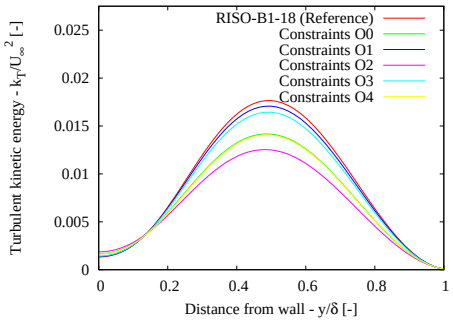

(c) Turbulent kinetic energy

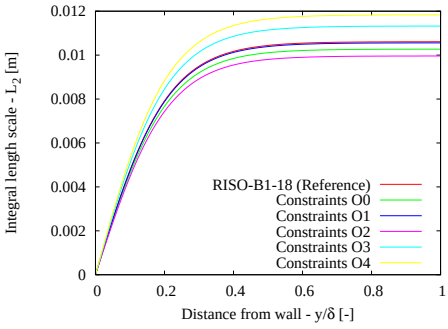

(d) Integral length scale

Figure 27. Boundary Layer Profiles at Trailing Edge (Suction side - $x/C = 0.995$)

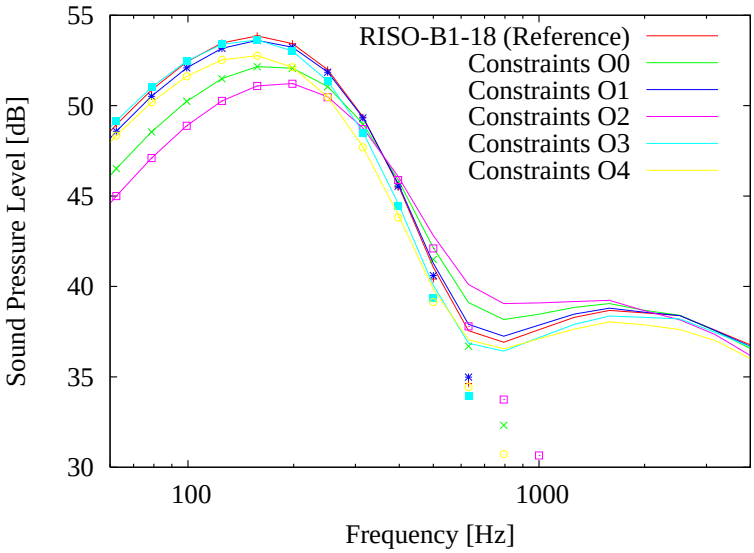

(a) Non-filtered SPL

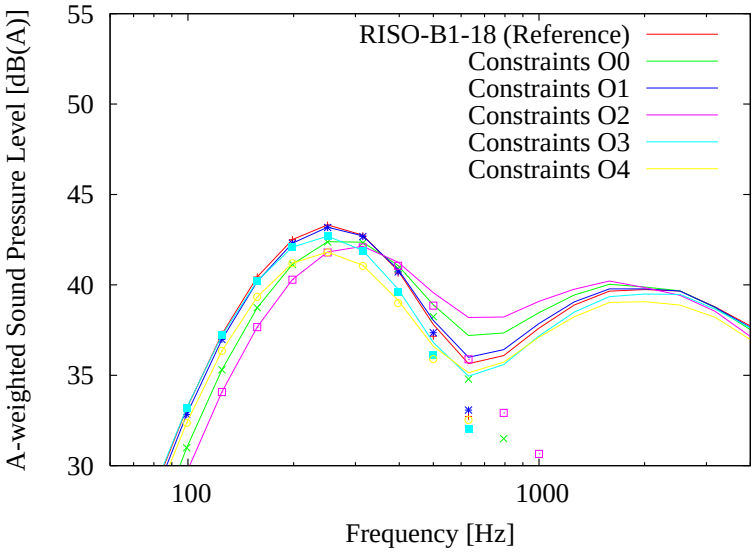

(b) A-weighted SPL

Figure 28. Sound Pressure Levels (Points: TNO model for suction side only)

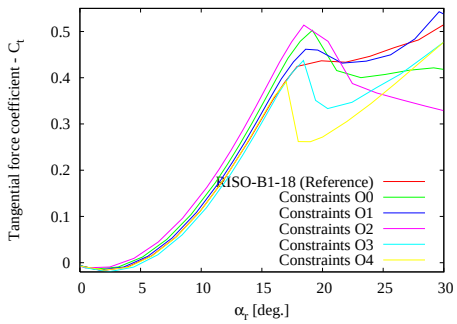

(a) Tangential coefficient

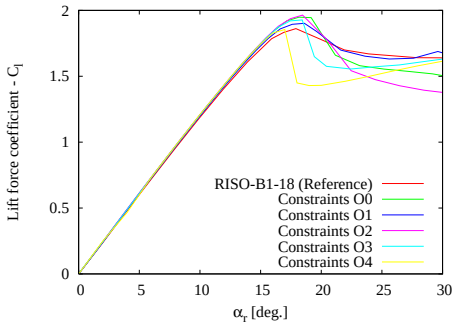

(b) Lift coefficient

Figure 29. Polar Characteristics

4.3 Airfoil Design - Reference Airfoil: S809

The second reference airfoil that is considered for our noise optimization tests is the S809 airfoil. It was designed at NREL by Somers [36] specifically for horizontal wind turbine applications. The airfoil was designed to have a sustained maximum lift, minimal sensitivity of lift to roughness, and low profile drag. It is chosen for our numerical optimization experiment as it is believed that this airfoil is more noisy than the RISØ-B1-18 considered in the previous section.

The cost function used in our optimization calculations involves only the maximum value of the A-weighted Sound Pressure Level for an angle of attack equal to $\alpha = 4^o$, which corresponds approximately to a relative angle of attack of $\alpha_r = 5.2^o$ (see previous section for the definition of the relative angle of attack). The different constraint sets used to generate the different noise-optimized airfoils are designated as follows:

- **O0**
  Suction side: $x_{tr}(\alpha_r = 15^o)/C < 0.06$

  $1.2 < C_l(\alpha_r = 17^o) < 1.5$
  $1.1 < C_l(\alpha_r = 26^o) < 1.9$

  $0.11 < C_t(\alpha_r = 9^o)$
  $0.225 < C_t(\alpha_r = 14^o)$
- **O1** No constraints on x_{tr} and :

  $1.15 < C_l(\alpha_r = 17^o) < 1.6$
  $0.95 < C_l(\alpha_r = 26^o) < 1.8$

  $0.105 < C_t(\alpha_r = 9^o)$
  $0.215 < C_t(\alpha_r = 14^o)$
- **O2** Same as O1 but:
  $0.095 < C_t(\alpha_r = 9^o)$
  $0.205 < C_t(\alpha_r = 14^o)$

All the above constraints involving the lift and tangential force coefficients are enforced in the fully turbulent calculation cases. In addition, a few geometrical constraints are enforced so that the trailing edge thickness doesn't collapse.

Fig.30 shows the different profiles obtained after convergence of the optimization procedure with the different optimization constraints presented above. The deviations from the original S809 profile are shown on Fig.31. The different input data corresponding to each design and extracted from XFOIL are shown in Figs.32-33. The far field SPLs are plotted on Figs.34(a-b), tangential and lift coefficients as a function of the relative angle of attack on Figs.35(a-b).

It can be seen on the geometry of the resulting airfoils is slightly modified by the optimization process. This indicates that the optimization algorithm has difficulties in reducing the cost function. Looking at the resulting A-weighted SPL of the optimized airfoil, it can be observed that all optimized airfoils result in a very similar noise level reduction. This reduction is quite small (in the order of 1 dB).

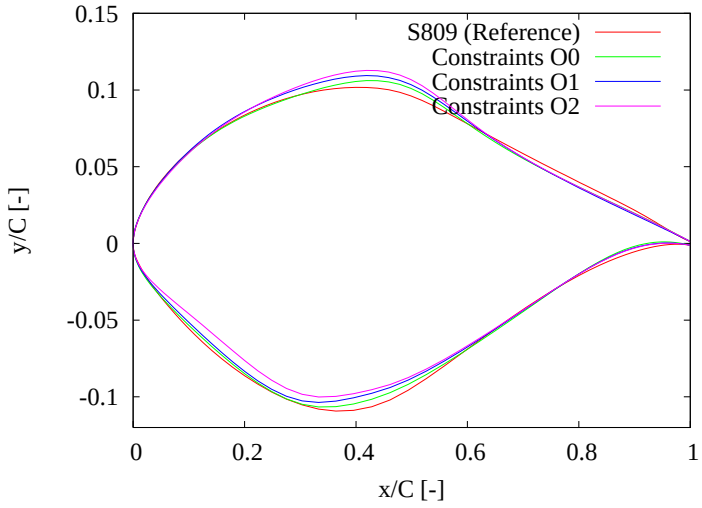

Figure 30. Airfoil Shapes

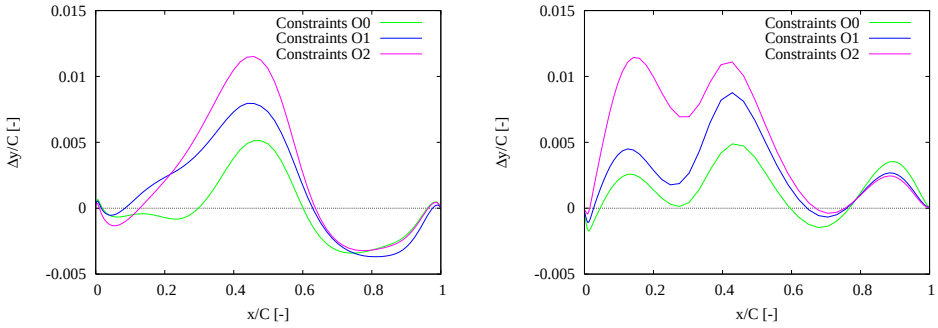

(a) Suction side (b) Pressure side

Figure 31. Optimized Airfoil Shape Deviations from S809

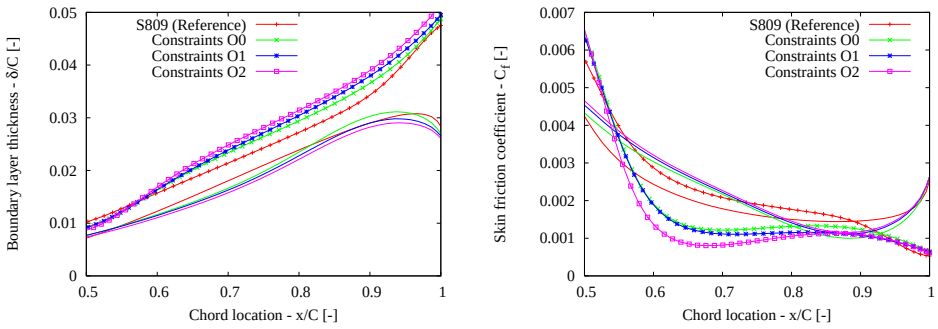

(a) Boundary layer thickness (b) Skin friction coefficient

Figure 32. Boundary Layer Characteristics
(Lines with points: Suction side; Lines without points: Pressure side)

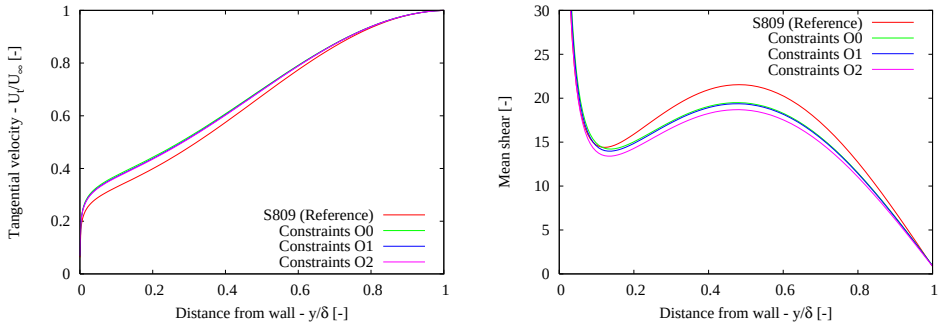

(a) Velocity profile

(b) Mean shear

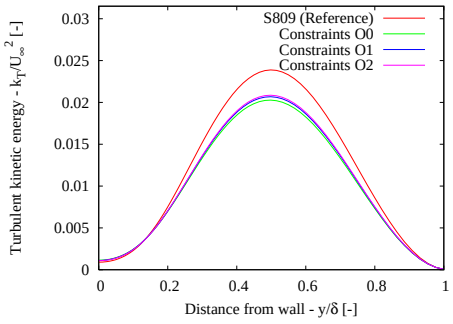

(c) Turbulent kinetic energy

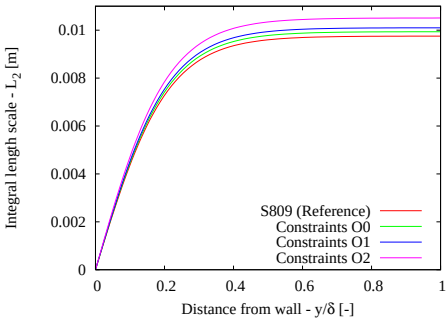

(d) Integral length scale

Figure 33. Boundary Layer Profiles at Trailing Edge (Suction side - $x/C = 0.995$)

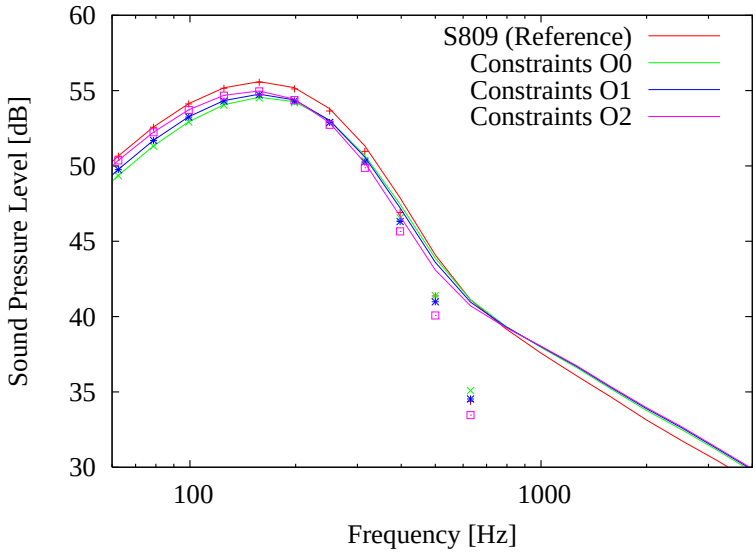

(a) Non-filtered SPL

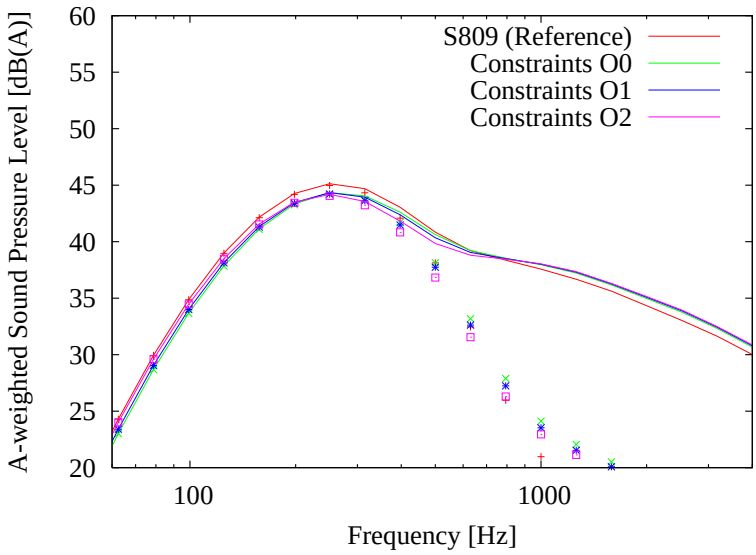

(b) A-weighted SPL

Figure 34. Sound Pressure Levels (Points: TNO model for suction side only)

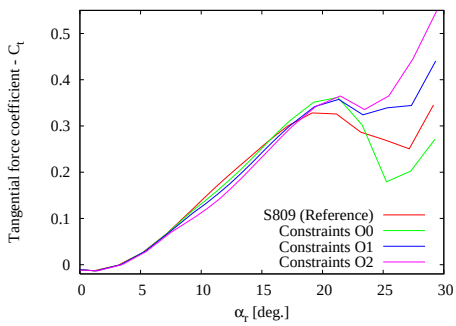

(a) Tangential coefficient

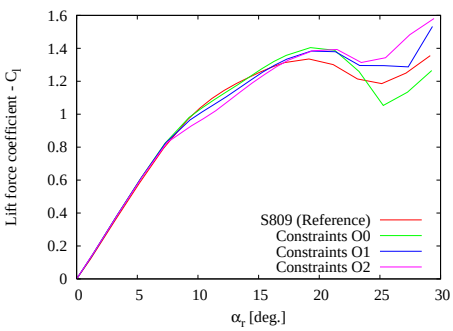

(b) Lift coefficient

Figure 35. Polar Characteristics

4.4 Conclusions on Airfoil Noise Optimization

As it was shown in this section, it seems quite difficult for the optimization procedure to significantly reduce the noise emitted by the considered airfoils. This could have several causes. A first possibility is that the original design of these airfoils is located near a local minimum of the cost function (which in our case is restricted to the maximum value of the A-weighted SPL). The optimization algorithm used in this study presents the potential risk to get trap near such a local minimum.

The second possibility is that the additional geometrical and aerodynamic constraints that were enforced during the optimization procedure do not allow for a greater noise reduction. However, these constraints could not be relaxed too much if one is interested in preserving at least some of the characteristics of the original airfoil.

From the previous numerical experiments, there does not seem to exist a clear tendency for which airfoil shape modification can reduce the trailing edge noise. It can however be observed that the largest shape deviations mainly occur before and near the mid-chord of the airfoil, and still have an influence on the trailing edge noise.

5 Conclusion

This work was in a first place aimed at reviewing trailing edge noise modelling, concentrating on the so-called TNO model originally developed by Parchen [1]. The theory behind this model is quite complex. It involves physical theories (related to diffraction problems), arduous mathematical developments, many assumptions related to the characteristics of the phenomenon, as well as many results from turbulence theory. It results in a model which is relatively simple to implement in conjunction with a boundary integral method such as XFOIL, or a RANS numerical code. The model was tested and compared to different results from the litterature. However, the model results do not seem to match very well with experimental data (at least for the cases considered in this study). To a certain extent, comparisons with CAA results were slightly more encouraging.

Nevertheless, it is believed that the qualitative results obtained with the previous model can be used with some confidence when comparing different airfoils relatively to each other. Therefore, the model was implemented within an optimization procedure which has been previously successfully used for airfoil design. It was found that an improvement of the noise characteristics of two different airfoils was possible. However, the gain obtained in term of far field Sound Pressure Level was quite low.

Acknowledgements

This work was carried out under a contract with the Danish Technical Research Council (STVF), Prediction and Reduction of Noise from Wind Turbines, 2004-2007. Computations were made possible by the use of the Linux cluster at the Risø central computing facility, and the computational resources of the Danish Center for Scientific Computing at MEK/DTU in Lyngby.

References

[1] Parchen, R., "Progress report DRAW: A Prediction Scheme for Trailing-Edge Noise Based on Detailed Boundary-Layer Characteristics", TNO Rept. HAG-RPT-980023, TNO Institute of Applied Physics, The Netherlands, 1998.

[2] Lighthill, M.J., "On Sound Generated Aerodynamically. I. General Theory", Proceedings of the Royal Society London, **A211**, pp.564-587, 1952.

[3] Brooks, T.F., Pope, S.D., and Marcolini, M.A., "Airfoil Self-Noise and Prediction", Tech. Rep., NASA Reference Publication 1218, Langley Research Center, 1989.

[4] Amiet, R.K., "Acoustic Radiation from an Airfoil in a Turbulent Stream", J. Sound Vib., Vol.41, No.4, pp.407-420, 1975.

[5] Amiet, R.K., "Noise due to Turbulent Flow Past a Trailing Edge", J. Sound Vib., Vol.47, No.3, pp.387-393, 1976.

[6] Ffowcs Williams, J.E, and Hall, L.H., "Aerodynamic Sound Generation by Turbulent Flow in the Vicinity of a Scattering Half Plane", J. Fluid Mech., Vol.40, Part 4, pp.657-670, 1970.

[7] Chase, D.M., "Sound Radiated by Turbulent Flow off a Rigid Half-Plane as Obtained from a Wavevector Spectrum of Hydrodynamic Pressure", J. Acoust. Soc. Am., Vol.52, pp.1011-1023, 1972.

[8] Chandiramani, K.L., "Diffraction of Evanescent Waves with Applications to Aerodynamically Scattered Sound and Radiation from Unbaffled Plates", J. Acoust. Soc. Am., Vol.55, No.1, pp.19-29, 1974.

[9] Howe, M.S., "A Review of the Theory of Trailing Edge Noise", J. Sound Vib., Vol.61, No.3, pp.437-465, 1978.

[10] Brooks, T.F., and Hodgson, T.H., "Trailind Edge Noise Prediction from Measured Surface Pressures", J. Sound Vib., Vol.78, No.1, pp.69-117, 1981.

[11] Blake, W.K., Mechanics of Flow-Induced Sound and Vibration, Vol.I and II, in Applied Mathematics and Mechanics, Frenkiel, F.N. and Temple, G. (eds.), Academic Press, 1986.

[12] Curle, N., "The Influence of Solid Boundaries upon Aerodynamic Sound", Proc. of the Royal Society, Vol.A321, pp.505-514, 1955.

[13] Ffowcs Williams, J.E, and Hawkings, D.L., "Sound Generation by Turbulence and Surfaces in Arbitrary Motion", Phil. Trans. Roy. Soc. **A264**, pp.321-342, 1969.

[14] Amiet, R.K., "Compressibility Effects in Unsteady Thin-Airfoil Theory", AIAA J., Vol.12, pp.253-255, 1974.

[15] Casper, J., and Farassat, F., "Broadband Trailing Edge Noise Predictions in the Time Domain", J. Sound Vib., Vol.271, pp.159-176, 2004.

[16] Corcos, G.M., "The Structure of the Turbulent Pressure Field in Boundary Layer Flows", J. Fluid Mech., Vol.18, pp 353-378, 1964.

[17] Chase, D.M., "Noise Radiated from an Edge in Turbulent Flow", AIAA J., Vol.13, No.8, pp.1041-1047, 1975.

[18] Howe, M.S., "Contributions to the Theory of Aerodynamic Sound, with Application to Excess Jet Noise and the Theory of the Flute", J. Fluid Mech., Vol.71, pp.625-673, 1975.

[19] Ffowcs Williams, J.E, "Surface-Pressure Fluctuations Induced by Boundary-Layer Flow at Finite Mach Number", J. Fluid Mech., Vol.22, pp.506-519, 1965.

[20] Drela, M., "XFOIL: An Analysis and Design System for Low Reynolds Number Airfoils", in Low Reynolds Number Aerodynamics, Mueller, T.J. (ed.), Lecture Notes in Engineering, Vol. 54, Springer-Verlag, Berlin, pp.1-12, 1989.

[21] Michelsen, J.A., "Basis3D - A Platform for Development of Multiblock PDE Solvers", Technical Report AFM 92-05, Technical University of Denmark, 1992.

[22] Michelsen, J.A., "Block Structured Multigrid Solution of 2D and 3D Elliptic PDE's", Technical Report AFM 94-06, Technical University of Denmark, 1994.

[23] Sørensen, N.N., "General Purpose Flow Solver Applied to Flow over Hills", Risø-R-827-(EN), Risø National Laboratory, Roskilde, Denmark, June 1995.

[24] Hinze, J.O., *Turbulence*, McGraw Hill, 1959.

[25] Schlichting, H., *Boundary Layer Theory*, McGraw Hill, 1968.

[26] Wagner, S., Guidati, G., and Ostertag, J., "Numerical Simulation of the Aerodynamics and Acoustics of Horizontal Axis Wind Turbines", Proc. of the 4^{th} European Comp. Fluid Dyn. Conf, Athens, Papailiou, K. (ed.), Vol.2, pp.436-441, 1998.

[27] Lutz, T., Herrig, A., Würz, W., Kamruzzaman, and Krämer, E., "Design and Wind-Tunnel Verification of Low-Noise Airfoils for Wind Turbines", AIAA Journal, Vol.45, No.4, pp.779-785 2007

[28] Herrig, A., Würz, W., and Wagner, S. "Silent Rotors by Acoustical Optimization (SIROCCO)", EU project SIROCCO, Deliverable D9, Tech. Report, Institute of Aerodynamic and Gas Dynamics, University of Stuttgart, 2003.

[29] Humpf, A., "Investigation of Computational Aeroacoustic Tools for Wind Turbine Aerofoils", Diploma Thesis, CENER, Sarriguren, Spain, 2006.

[30] Moriarty, P., and Migliore, P., "Semi-empirical Aeroacoustic Noise Prediction Code for Wind Turbines", Tech. Rep. NREL/TP-500-34478, National Renewable Energy Laboratory, Golden, Colorado, 2003.

[31] Zhu, W.J., "Aero-Acoustic Computations of Wind Turbines", Technical Report MEK-PHD 2007-09, Institute for Mechanics, Energy and Construction, Danish Technical University, Lyngby, 2008.

[32] Shen, W.Z., and Sørensen, J.N., "Comment on the Aeroacoustic Formulation of Hardin and Pope", AIAA Journal, Vol.37, No.1, pp.141-143, 1999.

[33] Shen, W.Z., and Sørensen, J.N., "Aeroacoustic Modelling of Low-Speed Flows", Theoret. Comput. Fluid Dynamics, Vol.13, pp.271-289, 1999.

[34] Fuglsang, P., and Dahl, K.S., "Multipoint Optimization of Thick High Lift Airfoil Wind Turbines", Proc. EWEC'97, Dublin, Ireland, pp.468-471, 1997.

[35] Fuglsang, P., and Bak, C., "Development of the Risø Wind Turbine Airfoils", Wind Energy, Vol.7, pp.145-162, 2004.

[36] Somers, D.M., "Design and Experimental Results for the S809 Airfoil", NREL/SR-440-6918, National Renewable Energy Laboratory, Golden, CO, 1997.

Risø's research is aimed at solving concrete problems in the society.

Research targets are set through continuous dialogue with business, the political system and researchers.

The effects of our research are sustainable energy supply and new technology for the health sector.